2011-10-26

Fabrication and Application of Vertically Aligned Carbon Nanotube Templated Silicon Nanomaterials

Jun Song
Brigham Young University - Provo

Fabrication and Application of Vertically Aligned

Carbon Nanotube Templated Silicon Nanomaterials

Jun Song

A dissertation submitted to the faculty of
Brigham Young University
in partial fulfillment of the requirements for the degree of

Doctor of Philosophy

Robert C. Davis, Chair
Richard R. Vanfleet
Gus L. W. Hart
Matthew R. Linford
Karine M. Chesnel

Department of Physics and Astronomy

Brigham Young University

December 2011

ABSTRACT

Fabrication and Application of Vertically Aligned

Carbon Nanotube Templated Silicon Nanomaterials

Jun Song

Department of Physics and Astronomy

Doctor of Philosophy

A process, called carbon nanotube templated microfabrication (CNT-M) makes high aspect ratio microstructures out of a wide variety of materials by growing patterned vertically aligned carbon nanotubes (VACNTs) as a framework and then infiltrating various materials into the frameworks by chemical vapor deposition (CVD). By using the CNT-M procedure, a partial Si infiltration of carbon nanotube frameworks results in porous three dimensional microscale shapes consisting of silicon-carbon nanotube composites. The addition of thin silicon shells to the VACNTs enables the fabrication of robust silicon nanostructures with flexibility to design a wide range of geometries. Nanoscale dimensions are determined by the diameter and spacing of the resulting silicon/carbon nanotubes while microscale dimensions are controlled by the lithographic patterning of CNT growth catalyst. The characterization and application of the new silicon nanomaterial, silicon-carbon core-shell nanotube (Si/CNT) composite, is investigated thoroughly in the dissertation.

The Si/CNT composite is used as thin layer chromatography (TLC) separation media with precise microscale channels for fluid flow control and nanoscale porosity for high analyte capacity. Chemical separations done on the CNT-M structured media outperform commercial high performance TLC media resulting from separation efficiency and retention factor.

The Si/CNT composite is also used as an anode material for lithium ion batteries. The composite is assembled into cells and tested by cycling against a lithium counter electrode. This CNT-M structured composite provides an effective test bed for studying the effects of geometry (e.g. electrode thickness, porosity, and surface area) on capacity and cycling performance. A combination of high gravimetric, volumetric, and areal capacity makes the composite an enabling materials system for high performance Li-ion batteries.

Last, a thermal annealing to the Si/CNT composite results in the formation of silicon carbide nanowires (SiCNWs). This combination of annealing and Si/CNTs yields a unique fabrication approach resulting in porous three dimensional silicon carbide structures with

ACKNOWLEDGMENTS

Contents

List of Figures

Chapter 1

Introduction

1.1 Nanomaterials

Nanomaterials are often defined as materials whose sizes in at least one dimension are significantly smaller than one micrometer. Nanomaterials usually include nanoparticles, nanowires, nanotubes, and nanoscale thin films. A nanoparticle is a particle whose diameter is less than 100 nm. Nanowires are solid materials in the form of wire with a diameter smaller than about 100 nm. A nanotube is a hollow nanowire. Thin films whose thickness is below 100 nm can be considered nanoscale thin films. Nanoparticles, nanowires/nanotubes, and nanoscale thin films are quasi zero dimensional, one dimensional, and two dimensional materials, respectively. Due to the unique size, nanomaterials have extraordinary fundamental mechanical, electronic, and thermal properties.[1–3]

The mechanical property of materials can be influenced by internal structural defects such as dislocations, micro twins, and impurity precipitates which are widespread in materials. By thermal annealing, imperfections in nanomaterials can easily migrate to the surface resulting in low defect densities inside the nanomaterials. The low defect density in nanomaterials can enhance the strength or ductility.[1]

The thermal properties of nanomaterials are also different from those of bulk materials. Heat is carried both by free electrons (and holes in semiconductors) and phonons. The scattering lengths of phonons and electrons are different, it is possible to realize phonon blocking and electron transmission by controlling the size of nanomaterials.[2] However, the thermal properties of nanomaterials have not been investigated thoroughly because it is difficult to control and measure the thermal conductivity of nanomaterials.[4]

The electronic and optical properties of nanomaterials deviate substantially from those of bulk materials. The energy band structure and corresponding optical properties in the materials can change significantly due to the quantum confinement of nanomaterials. In nanomaterials, the density of energy states will appear continuous near the center of the band but consists of discrete levels at the edges of the band. Metal conductivity is dominated by states at the Femi energy, but the band edges play a role in semiconductor conductivity. For this reason, the conductivity of semiconductors is more sensitive to nanoscale dimension than metals.[2]

Nanostructured materials are used in many applications. Nanowires can be potentially used in nanophotonics, laser, nanoelectronics, solar cells, energy storage, resonators, and high sensitivity sensors. Nanoparticles can be potentially used in catalysts, functional coatings, nanoelectronics, energy storage, drug delivery, and biomedicines. Nanoscale thin films can be used in light emitting devices, displays, and high efficiency photovoltaics.

1.1.1   Carbon Nanotubes

Carbon nanotubes (CNTs), a form of pure carbon, can be visualized as rolled hexagonal carbon networks that are capped by pentagonal carbon rings. There are two types of CNTs: single-walled carbon nanotubes (SWCNTs) and multi-walled carbon nanotubes (MWCNTs). SWCNTs consist of a single graphite sheet wrapped into a cylindrical tube with a diameter

from 1 nm to 5 nm. In contrast, MWCNTs comprise an array of tubes that are concentrically nested. The diameter of MWCNTs is typically from 6 nm to 100 nm. CNTs have been constructed with length-to-diameter ratio of up to 132,000,000:1.[5]

The discovery of carbon nanotubes has a complicated history.[6] The earliest research on carbon nanofibers was reported by L. V. Radushkevich and V. M. Lukyanovich in 1952($Soviet Journal of Physical Chemistry$).[7] However, the report did not attract attention possibly due to the Russian language. The first time hollow carbon fibers were observed by Oberlin, Endo, and Koyama by using high-resolution transmission electron microscopy (HRTEM) in 1976.[8]

In 1991 Sumio Iijima published a paper that initiated intensive research on CNTs.[9] In the report, Iijima synthesized helical carbon microtubules (now called nanotubes) by using an arc-discharge fullerene reactor. The nanomaterials consist of nested graphene tubules and were identified with HRTEM and electron diffraction. These concentric tubules exhibited interlayer spacings of ~ 3.4 Å, a value slightly greater than that of graphite (3.35 Å). Iijima associated this spacing difference to a combination of the graphene sheet curvature and weaker van der Waals forces acting between the successive cylinders.

In CNTs, carbon atoms exhibit sp2 hybridization, in which each atom is connected evenly to three carbons (120°) in the xy plane and a weak π bond is present in z axis. The C-C sp2 bond length is 1.42 Å. The sp2 hybridization forms a hexagonal lattice typical graphite sheet. Theoretically, it is possible to construct sp2-hybridized carbon tubule by rolling up a hexagonal graphene sheet and the rolling in different ways results in chirality variance including armchair, zigzag, and chiral configurations. Depending upon tube diameter, graphitization and chirality, carbon nanotubes can be either metallic or semiconducting with an electron mobility of 100,000 cm^2/(V·s).[10] Carbon nanotubes also have high stiffness and axial strength resulting from the high carbon-carbon sp2 bonding energy (113 kcal/mole).

The thermal conductivity of an individual SWCNT can reach up to 200,000 W/K compared to 3,000 W/K of graphite.[11]

Carbon nanotubes can be produced using a wide variety of processes such as arc-discharge, laser ablation, and chemical vapor deposition.

In the 1991 work by Iijima, an arc-discharge evaporation method was used to synthesize needle-like carbon tubes.[9] The carbon tubes, ranging from 4 to 30 nm in diameter and up to 1 mm in length, grew on the negative end of the carbon electrode. An arc-discharge chamber filled with a gas mixture of 10 Torr methane and 40 Torr argon was used, and two vertical thin electrodes were installed in the center of the chamber. The arc-discharge was generated by running a direct current (DC) of 200 A at 20 V between the electrodes. Both MWCNTs and SWCNTs can be synthesized by the arc-discharge evaporation method, but diameter and length of nanotubes are dependent on gas components, metal catalyst, current and pressure.[12]

In 1996, Smalley et al produced SWCNTs by laser-ablation (vaporization) of graphite rods with small amounts of Ni and Co at 1200 °C.[13] In the method, the CNTs kept growing until too many catalyst atoms aggregate on the top of nanotubes, which allows nanotubes to terminate with a fullerene-like tip or with a catalyst particle.

In 1996, a CVD process was used to produce CNTs with capability of controlling growth direction and synthesizing a large quantity of nanotubes.[14] In the process, a substrate with catalyst on it is put into a furnace reactor and heated up in an oxygen free environment. After a desired high temperature from 700 °C to 900 °C is reached, a mixture of hydrocarbon gas (acetylene, methane or ethylene) and nitrogen (or argon or helium) is introduced into the reactor at atmospheric pressure resulting in CNTs growth. The substrate is usually silicon, but some metals[15] and quartz[16] are also used. The catalysts, Fe, Co, and Ni, can be deposited on substrates from solution, electron beam evaporation, or sputtering. The

diameter and length of nanotubes depend on catalyst particle, temperature, growth time, and gases components.[17, 18]

In conclusion, CNTs are important low-dimensional nanomaterials because of their small diameter, high aspect ratio, high mechanical strength, high thermal and chemical stabilities, and excellent heat and electrical conduction. As a result, CNTs are promising materials in a variety of applications, such as fillers for polymer matrices, sensors, or field effect transistors.

1.1.2 Silicon Nanomaterials

Silicon nanostructure materials, including silicon thin film, silicon nanoparticles, silicon nanowires (SiNWs) and silicon nanotubes (SiNTs), have attracted attention due to interest in nanoscale properties such as light emission,[19] quantum confinement effects,[20] and energy storage.[21] In these nanostructure materials, SiNWs are expected to play a key role as interconnection and functional components in future silicon based nanosized electronic and optical devices.

In 1998, Morales and Lieber first synthesized nanoscale silicon wires with a laser ablation method.[22] In their work, laser ablation was used to prepare nanometer-diameter catalyst clusters that define the size of wires produced by vapor-liquid-solid (VLS) growth. This approach was used to prepare bulk quantities of uniform single-crystal silicon and germanium nanowires with diameters of 6 to 20 and 3 to 9 nanometers, respectively, and lengths ranging from 1 to 30 micrometers.

Since then, considerable effort has been devoted to synthesize SiNWs by VLS,[23] chemical vapor deposition,[24] laser ablation,[22] thermal evaporation,[25] template-assisted growth,[26] lithography related etching,[27] and oxide-assisted growth (OAG).[19] Presently, SiNWs are mainly applied in catalysis, Li ion batteries, solar cells, biological and chemical sensors.

1.2   Materials Characterization Techniques

To better understand the CNT templated silicon nanomaterials, I used precise characterization tools including atomic force microscopy (AFM), scanning electron microscopy (SEM), transmission electron microscopy (TEM), Raman spectroscopy, and electron energy loss spectroscopy (EELS).

1.2.1   Atomic Force Microscope (AFM)

In 1986, Binnig, Quate, and Gerber first demonstrated atomic force microscopy (AFM), which combined the principles of operation of STM and the stylus profilometer.[28] AFM is used for imaging, measuring, and manipulating matter with demonstrated resolution at the nanoscale.[29] An AFM has a cantilever with a sharp tip at its end. An AFM obtains an image of surface topography by using the tip to scan a sample surface and measuring the force between the tip and the sample surface. The force is typically from 10^{-11} N to 10^{-6} N and causes the cantilever to bend. The bending of the cantilever is monitored by a detection of the deflection of the laser beam at a quadrant photodiode. Typical cantilever spring constants are in range of 0.001-100 N/m. The deflection detector can measure motions from micrometers to 0.1 Å.

1.2.2   Scanning Electron Microscope (SEM)

A Scanning Electron Microscope (SEM) is a common tool for high resolution imaging, allowing displaying feature sizes of nanometers. In 1935, Max Knoll first produced a SEM image of silicon steel showing electron channeling contrast.[30]

A SEM is an electron microscope by using a high energy beam of electrons to scan a sample.[31] The electrons interact with the sample atoms to produce signals that contain

information about the sample's structure and composition. The signals include secondary electrons, back-scattered electrons (BSE), characteristic X-rays, specimen current and transmitted electrons. A wide range of magnifications are available, from about 10 times to more than 500,000 times.

1.2.3 Transmission Electron Microscopy (TEM)

In 1931, Max Knoll and Ernst Ruska invented the first Transmission Electron Microscope (TEM).[32] A sample used in TEM must be an ultra thin specimen, through which a beam of electrons can be transmitted. The interaction of electrons transmitted forms an image of the specimen, and the image is focused on a fluorescent screen or detected by a sensor such as a CCD camera. TEMs are able to produce images with a significantly high resolution owing to the small de Broglie wavelength of electrons. As a result, TEMs allow users to examine fine detail from two hundred nanometers to an angstrom scale magnification.[33,34] At low magnifications, TEM image contrast is dependent on the absorption of electrons in the material. At high magnifications complex wave interactions modulate the intensity of the image. Alternate modes in the TEM can obtain more material information including chemical identity, crystal orientation, electronic structure, and sample induced electron phase shift as well as the regular absorption based imaging.

Combined with a SEM or a TEM, Energy-dispersive X-ray spectroscopy (EDX) has been an analytical technique used for the elemental components or chemical characterization of a sample since 1960s. An incident beam on the surface of a sample may excite an electron from an inner shell bound to the nucleus, eject it from the shell and create a hole where the electron originally was. An electron from an outer, higher-energy shell then fills the hole, and the difference in energy between the higher-energy shell and the lower energy shell may be released in the form of an X-ray. The number and energy of the X-rays emitted from the

specimen can be measured by an energy-dispersive spectrometer.[35]

Combined with a TEM, an Electron Energy Loss Spectroscopy (EELS) is regarded as being complementary to EDX and was developed by James Hillier and RF Baker in 1944.[36] In EELS, a beam of electrons, with a narrow range of kinetic energies, is transmitted through the sample. Some electrons will lose energy and are deflected slightly and randomly after undergoing inelastic scattering. The lost energy can be measured via an electron spectrometer and interpreted in terms of what caused the energy loss. One can determine the types of atoms and the numbers of atoms of each type by carefully comparing the energy loss spectroscopy with the reference.[37]

1.2.4 Raman Spectroscopy

A Raman effect is the inelastic scattering of a photon, named after one of its discoverers, Sir.C.V.Raman. In 1934, George Placzek developed the theory of Raman effects.[38]

Typically in the Raman measurement, a sample is illuminated with a laser beam. The laser beam can result in molecular vibrations, phonons or other excitations which makes the energy of the laser photons shift up or down. The shift in energy gives information about the vibrational modes in the sample. Light from the illuminated spot is collected with a lens and sent through a monochromator. Wavelengths close to the laser line are filtered out while the rest of the collected light is dispersed onto a detector.[39]

1.3 Lithium Ion Battery Background

Lithium-ion batteries are energy-storage devices which convert chemical energy into electrical energy by electrochemical reduction and oxidation reactions. In this dissertation, only rechargeable lithium-ion batteries are discussed. A rechargeable lithium-ion battery contains

one anode, one cathode, and electrolyte. The anode is the negative electrode from which electrons are generated to do external work. The cathode is the positive electrode where positive ions migrate toward the LiMO layer structure (M stands for metal). The electrolyte allows lithium ions, not electrons, to flow from one electrode to another. The electrolyte is a liquid solution containing a salt dissolved in a solvent. The electrolyte must be stable in the presence of both electrodes. During the discharge process, lithium ions depart from the negative electrode, diffuse and migrate to, and intercalate into the positive electrode. The electrons are released from the negative electrode and move to the positive electrode through the external circuit. The reverse procedure occurs during the charge process.

The typical cathode materials of lithium-ion batteries are principally transition metal oxides such as $LiCoO_2$, $LiNiO_2$, or $LiMn_2O_2$.[40] $LiMn_2O_2$ is ideal for intercalation of small ions such as H^+ and $Li^{+2}O_4$. Its other advantages include low cost,high thermal threshold, excellent rate capability, and minimal health and environmental impacts.The standard anode material is carbon. Silicon is an interesting alternative to carbonaceous anodes. Silicon has the highest known specific lithium energy storage capacity at 4,200 mAh/g,[41] which is 10 times larger than in traditional carbonaceous anode materials. It is also the second most abundant element on the earth's crust. As a result, it is very attractive as a potential lithium-ion battery anode material.

However, with this large capacity comes a large capacity fade during initial cycling and a volume change of as much as 400 %.[42] Several methodologies have been adopted to overcome the problem: one of these approaches is to replace bulk powders with thin films.[43,44] The thin films allow for volume expansion and strain relaxation, but thin film thickness has an effect on both the rate capability and cycling stability. An other approach is to increase the free space which can accommodate the volume variations by using silicon nanoparti-cles,[45,46] silicon nanowires (SiNWs), or silicon nanotubes (SiNTs).[21,47,48] Reducing the size

of particles or limiting the dimension of materials does not control the volume expansion but increases the stability presumably because of strain relaxation and more uniform expansion. Silicon nanoparticles below 20 nm in diameter exhibit a capacity up to 3467 mAh/g at C-rate C/5.[45] C-rate is defined by the capacity of electrodes, for example for 1C, the current is chosen for pure silicon such that I = silicon mass $\times$ capacity(4200 mA/g). SiNWs were applied as lithium battery anodes which exhibit a capacity up to 4000 mAh/g at a C-rate C/20,[21] which also makes possible to have more active materials per area. Since 2008, SiNWs and SiNTs have been investigated thoroughly for application to lithium ion batteries, including the influence of diameters,[49] dopant[50] and carbon coating.[47] Another approach is to form silicon-carbon nanocomposites by using carbon nanotubes or nanofibers. The Si-C nanocomposites were found to be effective in reducing capacity degradation during cycling.[51–53] Though carbon nanotubes have a relative high energy barrier restricting themselves as active materials in lithium ion batteries,[54] they are promising active matrices due to their nano-scale and good conductivity. Cui et al, spread carbon nanofibers (CNFs) on stainless steel foils and deposited silicon onto CNFs by a CVD procedure.[51] Kumta et al, grew carbon nanotubes (CNTs) on the glass, deposited silicon onto CNTs, and transferred the Si/CNT nanocomposites to copper foils.[52]

All work above has achieved much higher gravimetric capacities than carbonaceous anode by using silicon anode. However, to realize high capacity batteries, high areal and volumetric capacities are as critical as gravimetric capacities. My work in Chapter 4 focuses on an approach using silicon-CNT composites to achieve a combination of high gravimetric, volumetric, and areal capacity. Chapter 4 has been written up as a journal article and is in review at the Journal of Electrochemical Society.

1.4   Thin Layer Chromatography

Chromatography can be defined as "a physical method of separation in which components to be separated are distributed between two phases, one of which is stationary (stationary phase) while the other (the mobile phase) moves in a definite direction". Stationary phase is a solid or a liquid supported on a solid support surface, and mobile phase is a gas, liquid, or a supercritical fluid flowing over the stationary phase. The physical and chemical natures of these two phases determine the characteristics of a chromatographic separation. Chromatography is often used for separation, extraction, and analysis of various constituents, or fractions, of a sample interested. Chromatography may also be used for the preparation, purification, concentration, and clean-up of samples.

Thin layer chromatography (TLC) technique is a typical chromatography that separates molecule mixtures.[55] A TLC plate is usually a sheet of glass, plastic, or aluminum foil with a coating of adsorbent materials, such as silica gel, aluminum oxide, or cellulose. The adsorbent materials are used as the stationary phase, and a solvent carrying mixtures is regarded as a mobile phase. When mixtures and a solvent are applied on the plate, capillary action will pull the solvent upward along the plate. Because different analytes ascend the TLC plate at different rates, separation is achieved.

Today, commercial TLC plates are fabricated by coating glass or metal surfaces with porous silica microparticles. The microparticles are deposited on the surface under carefully controlled processes and held together with a binder (e.g., gypsum or polyvinyl alcohol). However, there is room to improve separation resolution and speed in TLC plates. The control of structure on the microscale is one of the solutions to the problem. Furthermore, though microscale structures have previously been fabricated for chromatography, the lack of nanoscale porosity limits the capacity of these structures. Here we applied the CNT-M process to fabricate TLC media with high degree control microscale geometry. The work is

described in Chapter 3 and was written up as a journal article and published in Advanced Functional Materials.

1.5 Significance of the Dissertation

A novel nanostructured material, silicon-carbon core-shell nanotube (Si/CNT) composite, is explored thoroughly in this dissertation including synthesis, characterizations, and applications of this material.

1. Fabricated silicon-carbon nanotube composites

   The Si/CNT composite has a high aspect ratio in three dimensions resulting in large surface area. The controllable diameters, heights, patterning and crystallization of the materials are useful in many applications. The achievements were published in Advanced Functional Materials (J. Song et al. Carbon-Nanotube-Templated Microfabrication of Porous Silicon-Carbon Materials with Application to Chemical Separations. Advanced Functional Materials 21, 1132-1139, 2011;

2. Applied to thin layer chromatography

   The patterned Si/CNT composite was oxidized and used as TLC media. The precise pattern of the composite improves fluid flow control and nanoscale porosity of the composite provides high analyte capacity. The chemical separations media outperformed commercial HPTLC plates. The achievements were published in Advanced Functional Materials (J. Song et al. Carbon-Nanotube-Templated Microfabrication of Porous Silicon-Carbon Materials with Application to Chemical Separations. Advanced Functional Materials 21, 1132-1139, 2011;

3. Applied to lithium ion batteries

The composite was used as anode materials in lithium ion batteries, and resulted in a combination of high gravimetric, volumetric, and areal capacity and is ideal for high performance Li-ion batteries. The achievements were submitted to Journal of Electrochemical Society;

4. Synthesized silicon carbon nanowires

The composite was annealed in a high-temperature environment with argon. The composite was converted to a wide band gap semiconductor material, silicon carbide nanowires (SiCNWs), with keeping three dimensional patterning as original. The achievement is being prepared for submission to Nanotechnology.

Chapter 2

Microfabrication procedure and characterization of silicon-carbon core-shell nanotubes

2.1 Introduction

Nanostructured silicon materials including silicon nanowires (SiNWs)[22] and silicon nanotubes (SiNTs)[56] have attracted attention due to interest in future silicon based nanodevices and nanoscale properties such as light emission[19] and quantum confinement effects.[20] SiNWs or SiNTs can be prepared by either physical or chemical methods. However for some applications, for example, in lithium-ion battery anodes[21] and hydrogen storage devices[57] the lithium or hydrogen ions require more accommodation sites and smoother transfer pathways, so the improved control of length, diameter, crystallization, and patterning of nanowires/nanotubes is needed. Although considerable effort has been devoted to developing controlled synthesis of silicon nanostructure materials, the precise control of large-scale formation of a well-aligned

forest is still elusive.

2.2   Synthesis of Vertically Aligned Carbon Nanotubs

In general, chemical vapor deposition (CVD) improves yield and purity of CNTs, allows for various substrates, and produces vertically aligned CNTs.[15] As a result, the CVD technique is widely used to grow CNTs today.
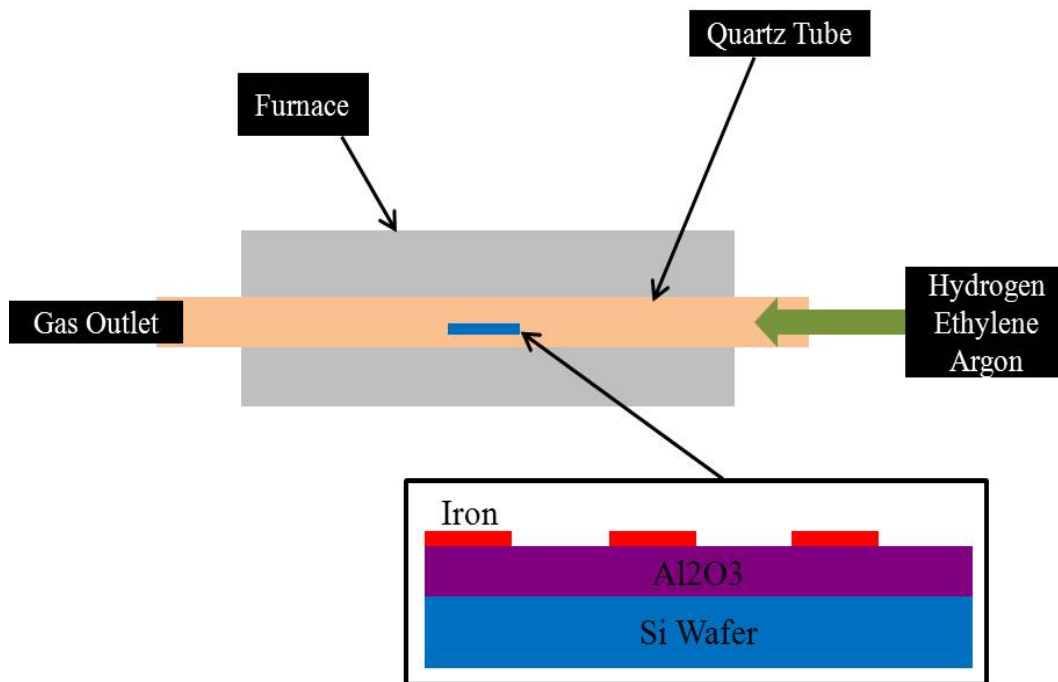
Figure 2.1 A diagram of a CNT growth instrument and a prepared substrate

In our work, CVD carbon nanotube synthesis consists of a three-step process. The first step is preparation of patterns on substrates. To realize a pattern, lithography technology can be used including e-beam lithography or photolithography. The pattern features sizes that are determined by the lithography can be as small as a few nanometers to as large as several centimeters. Photolithography was used due to its low-cost and efficiency. The

second step is deposition of a catalyst stack consisting of alumina and iron. The catalyst is critical to the nanotube synthesis in the sense that the diameter of CNTs depends on the size of catalyst clusters.[17] A thin film of alumina is deposited on patterned substrates using an e-beam evaporator, and then a thin film of iron is deposited on patterned substrates with alumina using a thermal evaporator. The thin film of alumina is used as a barrier layer between substrates and iron, and the thin film of iron is the active catalyst for CNTs growth. After the depositions of the thin films, a lift-off process removes photoresist which results in a patterned catalyst layer. The final step is to grow CNTs on the substrate in a carbon-rich gaseous environment. Normally, we put the substrates into a quartz tube heated up by a furnace with hydrogen. When the desired temperature (750 °C) is achieved, vertically aligned CNTs (VACNTs) are grown with the flowing mixed gases of ethylene and hydrogen. Cooling is done under argon. The as-grown nanotubes have diameter ~ 10 nm and the length can be several microns to millimeters dependent on CNTs growth time. The diagram of a CNT growth instrument and a prepared substrate is shown in Fig. (2.1).

CVD CNT synthesis involves many parameters such as hydrocarbon, catalyst, temperature, pressure, gas flow rate, deposition time, and reactor geometry. The parameters can influence diameter, length, growth speed, and alignment of CNTs. In this dissertation, the VACNTs will be used as a template to fabricate vertically aligned silicon nanomaterials, so the alignment and length are critical. Based on our experiment results and literature research,[58] catalyst is the most important for the alignment and length of CNTs. The investigation to thickness of catalyst is shown in Fig. (2.2). The roughness of a 10 nm alumina thin film is ~ 37 nm (Fig. (2.2)a), while the roughness of a 30 nm alumina thin film (Fig. (2.2)d)is ~ 3 nm. After 0.6 nm iron deposition and annealing in hydrogen, the surface morphology did not change significantly. With same quantity of iron, the VACNT growth is good in either speed or orientation when the alumina film thickness was over 10 nm. The standard

As-deposited Al_2O_3 (10nm)

Iron(0.6nm) on Al_2O_3 (10nm)

Annealed Iron(0.6nm)/Al_2O_3 (10nm)

As-deposited Al_2O_3 (30nm)

Iron(0.6nm) on Al_2O_3 (30nm)

Annealed Iron(0.6nm)/Al_2O_3 (30nm)
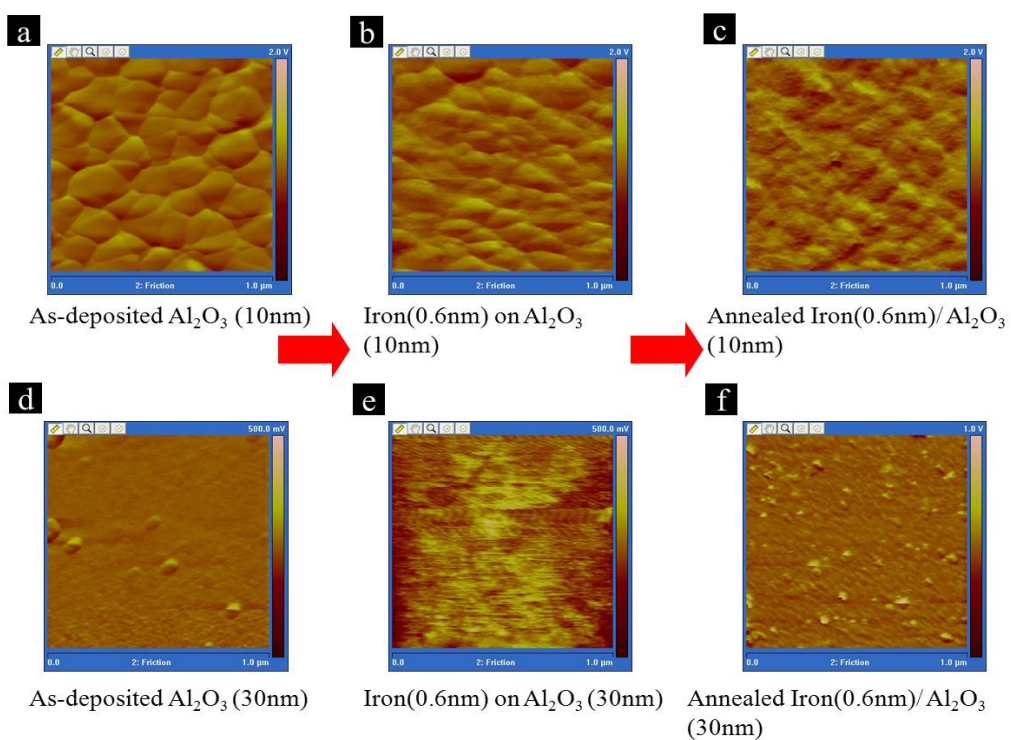
Figure 2.2 AFM images of catalyst layer with various thick alumina of 10 nm (a-c) and 30 nm (d-f). Alumina thin film 10 nm thick (a) and 30 nm thick (d); 0.6 nm iron was deposited on alumina (b,e); surface morphology after annealing with hydrogen (c,f)

good VACNT growth is shown in Fig. (2.3), which shows SEM images of VACNTs with a catalyst layer consisting of 2 nm iron on 30 nm alumina. A grid-patterned VACNTs is shown in Fig. (2.3)a, and a close-up view of VACNTs is shown in Fig. (2.3)b.
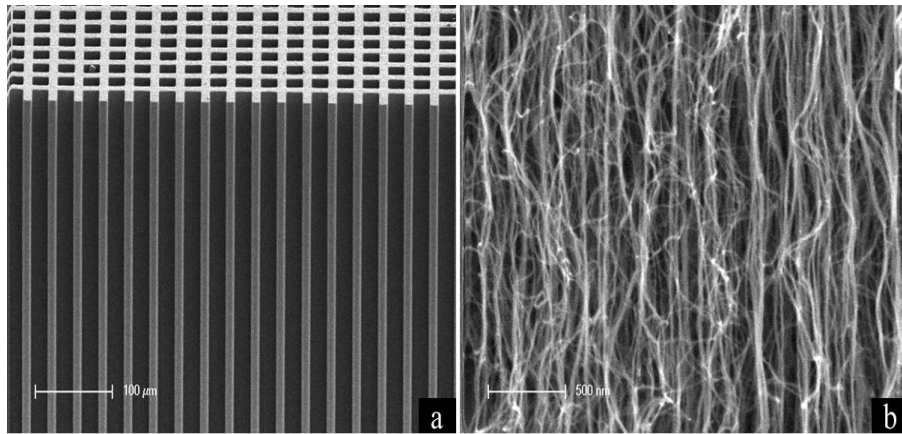
Figure 2.3 SEM images of VACNTs. (a) CVD synthesis of patterned CNTs on a silicon wafer. (b) a close-up view of VACNTs.

2.3 Fabrication of Silicon-Carbon Core-Shell Nanotubes

Low Pressure Chemical Vapor Deposition (LPCVD) silicon forms remarkably uniform films around patterned multi-walled carbon nanotubes (MWCNTs); Fig. (2.4) shows typical SEM images of patterned silicon-carbon core shell nanotube (Si/CNT) structures. Silicon was deposited onto the nanotubes by LPCVD where Silane (20 sccm) reacted with the specimen at an elevated temperature and low pressure (150 mtorr). The Si/CNTs are vertically aligned and retain the vertical orientation of the initial CNT forest. Complex 3D structures and lines of vertical Si/CNTs are shown in Fig. (2.4)a and (2.4)b. The height of the synthesized Si/CNTs is controlled by varying the run time for carbon nanotube growth. For example, 2 min growth resulted in 100 μm high CNTs.

The Si/CNT diameters can be from 10 nm to 120 nm, which depends on the LPCVD

process parameters and time. Fig. (2.4)c and (2.4)d are close-up views of Si/CNTs with thinner ((2.4)c) and thicker ((2.4)d) silicon films deposited at 530 °C and 560 °C for 60 mins. The 560 °C LPCVD deposition has a higher deposition rate and therefore grows a thicker silicon coating. The structure of the Si/CNTs is generally vertical with individual nanotubes in the structure following an undulating path, as seen in Fig. (2.4)c and (2.4)d.
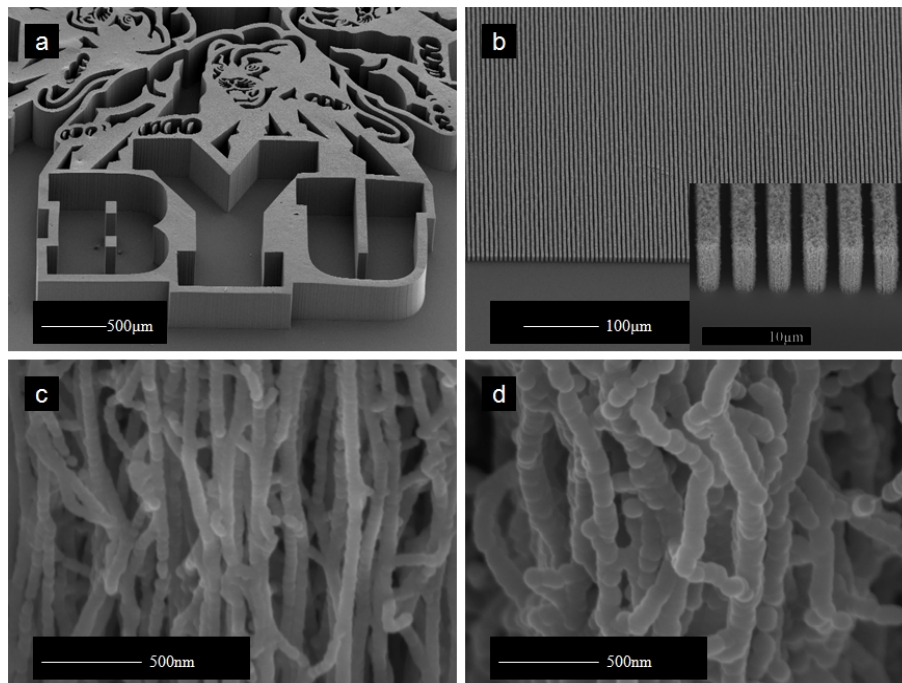
Figure 2.4 SEM images of patterned Si/CNTs. (a) An arbitrary 2D catalyst pattern results in a robust 3D Si/CNT structure, in this case a 400 μm high BYU logo. (b) Lines of 10 μm tall vertical Si/CNTs are shown. The close-up views of (b) are shown in the inset. (c) High magnification view shows Si/CNTs synthesized with LPCVD silicon at 530 °C for 60 min, which deposits a thin Si coating and results in 70 nm diameter Si/CNTs. (d) Si/CNTs synthesized with LPCVD silicon at 560 °C for 60 min, which deposits a thicker Si coating and results in 120 nm diameter Si/CNTs

2.4 Characterization of Silicon-Carbon Core-Shell Nanotubes

The structural characteristics of Si/CNTs were investigated by Raman spectroscopy. The Raman spectra of vertically aligned Si/CNTs are shown in Fig. (2.5) for both amorphous and crystalline samples. The amorphous silicon peak is centered at 465 cm^{-1} and seen in Fig. (2.5)a and (2.5)b. Because of the amorphous structure, the momentum selection rule is relaxed, and a broad peak is seen. In crystalline silicon, only the 64 meV optical phonon is allowed[59] resulting in a sharp peak at 517 cm^{-1} and a broad feature at 945 cm^{-1} seen in Fig. (2.5)c. The peak at 517 cm^{-1} of crystalline Si/CNTs is slightly broader, and more asymmetric than that of bulk silicon, which is consistent with Raman measurements of silicon nanowires.[60,61] All three Raman spectra show the first order D band (1305 cm^{-1}) and G band (1587 cm^{-1}) of carbon nanotubes. Increasing the thickness of silicon gives a corresponding increase in the silicon signal and decreases the CNT signal. Additionally, the relative intensities of the D and G bands change as the silicon thickness is increased. One question is whether a SiC layer was formed at the Si-CNT interface. SiC has many polytypes which have different Raman spectra. The maximum intensity folded transverse optical (FTO) modes for all 6 polytypes[62] fall in the range between 764 and 796 cm^{-1}, but there are no features in our spectra in this range indicating that within the detection limits of this instrument, there is no SiC present. Panitz et. al[63] have used Raman in the wavelength range from 250 to 1000 cm^{-1} to distinguish silicon carbide from silicon; our spectra are an excellent match to their silicon spectra including the broad feature just below 1000 cm^{-1}.

A series of transmission electron microscopy (TEM) images of Si/CNTs are shown in Fig. (2.6). The TEM images show two silicon morphologies after silicon deposition, either as beads formed along the CNT or a conformal shell of silicon over the CNT. Fig. (2.6)a
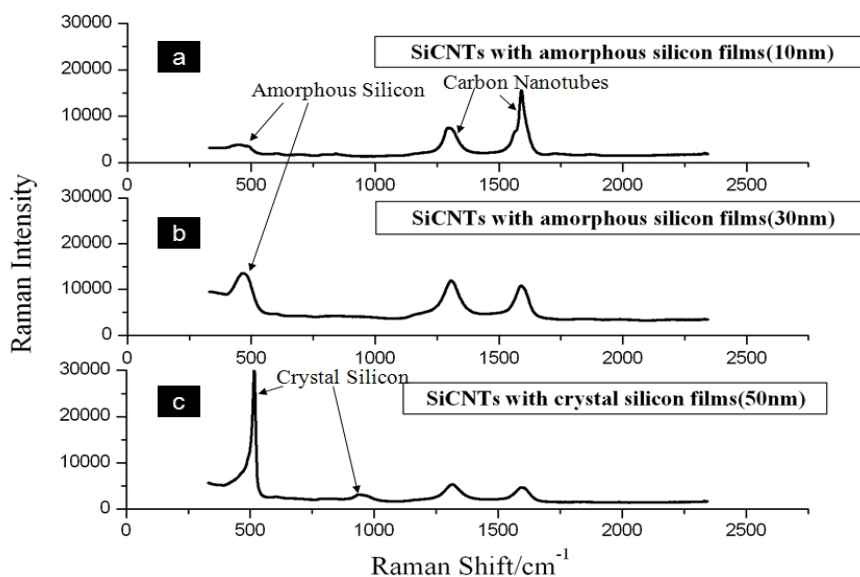
Figure 2.5 (a,b) 10 nm and 30 nm of amorphous silicon deposited at 530 °C. Raman spectrum peak of amorphous silicon is shown. With a thicker silicon shell, the peak of silicon (around 465 cm^{-1}) is higher; (c) 50 nm of crystalline silicon deposited at 560 °C and annealed at 700 °C overnight. Raman shifts of 517 cm^{-1} and 945 cm^{-1} indicate a crystalline silicon coating. Carbon nanotubes are identifiable in all spectrum (a,b,c)

and its inset show typical images where the multi-walled carbon nanotube core and the $\sim$ 10 nm (average) silicon coating can be seen. The fairly uniform silicon coating on these carbon nanotubes gives 30 nm wide Si/CNTs with occasional bead formation. At 530 °C, amorphous silicon was deposited on the nanotubes and above 560 °C polycrystalline silicon was deposited. The high resolution micrographs (Fig. (2.6)b is an amorphous silicon coating and Fig. (2.6)c is a crystalline silicon coating) show the morphology of these Si/CNTs, and the inset in Fig. (2.6)c shows the selected-area electron diffraction (SAED) pattern of that specimen showing its polycrystalline nature. To attain a uniform crystalline silicon coating, amorphous silicon was deposited at 560 °C and then thermally annealed at 700 °C for 12-14 hours.
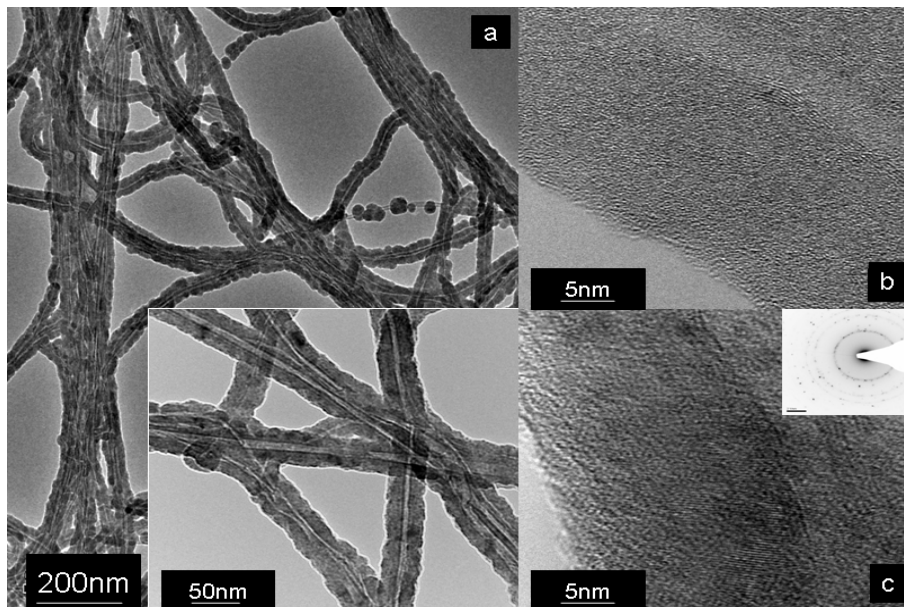
Figure 2.6 (a) TEM images of Si/CNTs with a 10 nm silicon coating are shown. The inset shows an enlarged view of Si/CNTs. (b) The high magnification image shows the morphology of Si/CNTs coated with amorphous silicon. (c) Polycrystalline silicon coated carbon nanotubes is proved by the SAED (Inset in c)

Scanning transmission electron microscopy (STEM) images and electron energy-loss spec-

troscopy (EELS) data are shown in Fig. (2.7). In Fig. (2.7)a, the annular dark field image shows a horizontally oriented Si/CNT. The core-shell structure seen in projection should have a dip in intensity at the carbon core as seen. The line on Fig. (2.7)a is the location of the EELS line scan shown in Fig. (2.7)b and Fig. (2.6)c. In Fig. (2.7)c, an EELS spectrum is shown from the middle of the Si/CNT. In the data shown, the decreasing background has been fit to the region before the silicon edge and subtracted from the entire spectrum. The silicon peak is just above (higher energy loss) the background window. The fine structure of the silicon peak is consistent with crystalline silicon. The carbon peak is also labeled on the right half of the spectrum and its fine structure is consistent with that of carbon nanotubes.[64] In the middle of the spectrum is an artifact that arises from a mismatch between the quadrants of the EELS CCD readout. We include the full spectrum (with artifact) to show that the silicon and carbon data come from the same data set with perfect spatial registry. With the background subtraction as shown in Fig. (2.7)c, the counts in the silicon peak (over some region close to the edge onset) are proportional to the number of silicon atoms seen by the beam. Fig. (2.7)b shows the number of counts in the silicon edge along the line scan. Also in Fig. (2.7)b, the carbon edge counts are shown. The carbon data used the same data sets but with the background subtraction taken just before the carbon edge, and the counts were then collected from near the carbon edge onset. The two lines in Fig. (2.7)b show the distribution of silicon and carbon across the Si/CNT. The silicon shows a dip in the middle of its distribution with a corresponding increase in carbon at the edges of the dip. Carbon also shows a dip in the middle of its distribution. This profile is what would be expected from the "tube" nature of both the silicon and CNT structure.
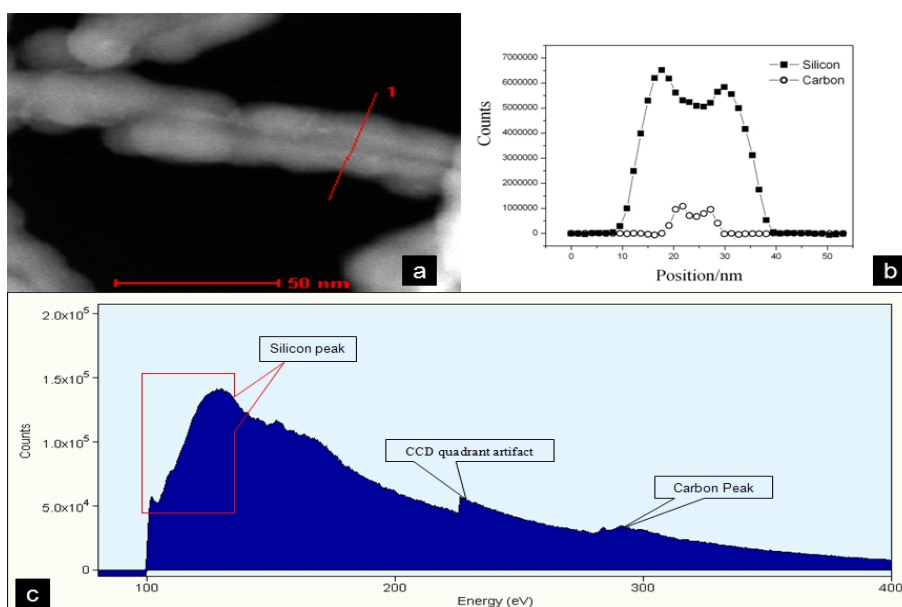
Figure 2.7 (a) Dark field image of an individual Si/CNT by STEM. An EELS measurement is made at each point as the beam is scanned through the Si/CNT along red line 1. (b) Counts above background in the Si and the C peaks are plotted vs. position along this scan line. The percentage of silicon and carbon varies along this cross-section of the Si/CNT. (c) EELS near the core of the Si/CNTs shows both silicon peaks and carbon peaks (from CNTs)

2.5   Mechanism of Silicon Infiltration

LPCVD is known to produce conformal coatings with excellent penetration into cracks and porous structures. Our results also show excellent penetration into the CNT forest, though the thickness and morphology of the silicon coating, under the conditions used, does depend somewhat on depth (and distance from the pattern edges) into the carbon nanotube forest, as shown in Fig. (2.8). The Si coating of the CNTs is compared between the top (a) and bottom (b) regions of the forest. In Fig. (2.8)a, the top region shows a uniformly thick coating, in Fig. (2.8)b the thinner coating is generally smooth, but in places it is discrete like beads on a string. Fig. (2.8)c plots the Si/CNT diameter at various depths in the structure showing that deep in the structure the deposition rate is lower. We define the diameter of Si/CNTs as the average width of tubes (top of the forest) or beads (bottom of the forest). The average diameter of Si/CNTs ranges from 48 nm on the top to 40 nm at the bottom for this deposition. The diameter and morphology variance arises from differences in the silicon deposition rate from the top to the bottom. To determine the difference in silicon deposition rate, we calculate the silicon volume per nanotube length using equation (2.1).

$$V/L = \pi(R^2 - r^2)C/L \tag{2.1}$$

In the formula above, V/L is the silicon volume per unit length of nanotube, R is the radius of the Si/CNTs, r is the radius of the CNTs, and C is the fraction of the nanotube length coated with silicon. All parameters here are illustrated in the Fig. (2.8)d. From an analysis of the 40 min Si deposition at 530 °C shown in Fig. (2.8)a and (2.8)b, V/L on the top is about 1750 nm^2, and at the bottom of the 400 μm forest V/L is about 900 nm^2, approximately half of that on the top.

To achieve uniform Si/CNT diameters, the deposition rate is expected to be limited by the kinetics of surface growth rather than the transport of gases to and from the CNT
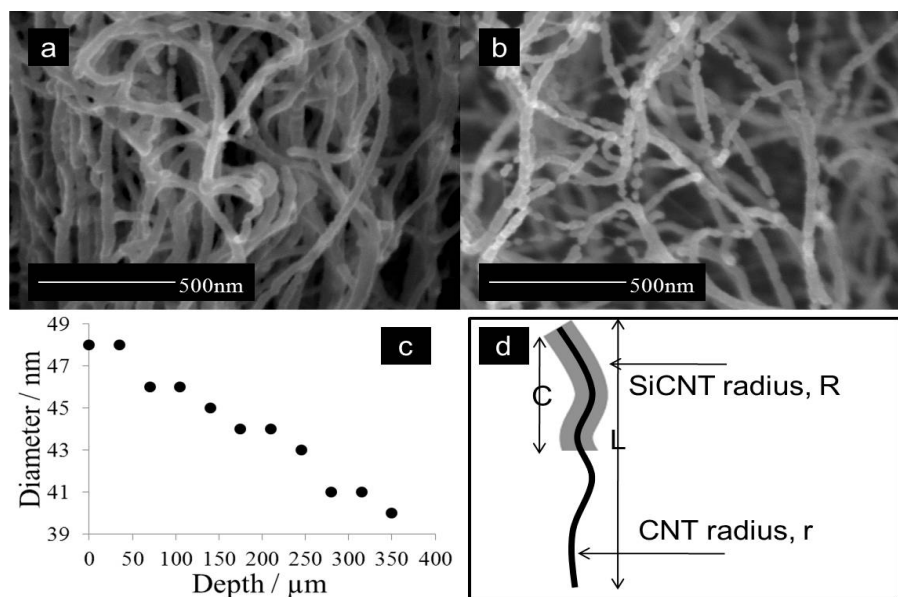
Figure 2.8 An un-patterned CNT forest was grown to a height of 400 μm and coated with silicon at 530 °C for 40 min. (a) The SEM image of the top of Si/CNTs shows a uniform coating. (b) The morphology of most tubes near the bottom is smooth, but there also are some discrete silicon beads. (c) The Si/CNT diameter is measured at various depths in the structure. The diameter of Si/CNTs decreases and more beadlike morphology is seen at greater depths. (d) A sketch shows parameters used to calculate the volume of deposited silicon

surface. The former is determined by an adsorption on the CNT surface, but the latter is related to a concentration change in a CNT forest. A model is set up to investigate Si/CNT diameter variance from the top to the bottom of a Si/CNT forest. In the model, from the top to the bottom of a CNT forest, the surface growth rate on CNTs is assumed consistent but the concentration of silane vapor is not. The Fig. (2.9) is a model sketch for an infiltration process, where a sample including the CNT forest on substrate is laid in the reactor. The height of the CNT forest is h, and coordinate is from the top (z=0) of CNTs to the bottom (z=h) of CNTs. The vapor comes from one side to the other side, which has a constant concentration at z=0 but varies from z=0 to z=h. The substrate forms a boundary condition which no diffusing species can pass through the z=h line.
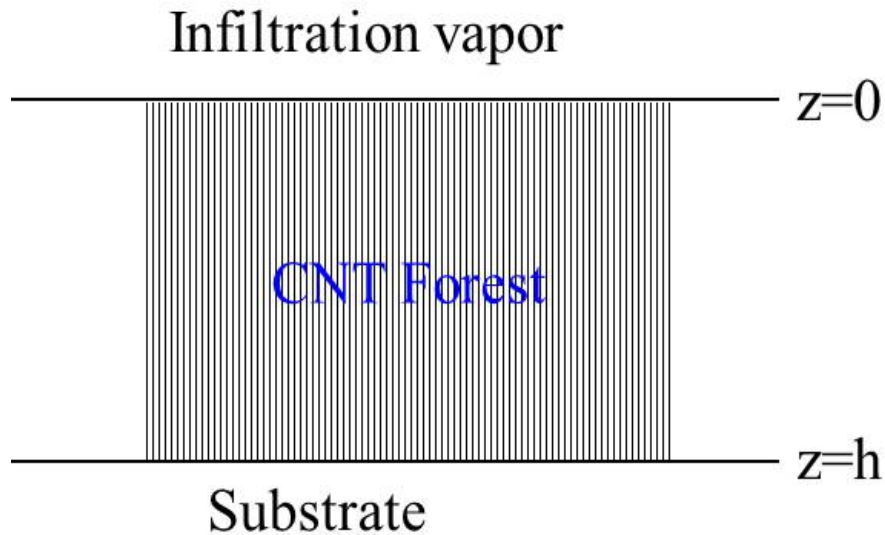
Figure 2.9 A infiltration process diagram for a theoretical study

Fick's second law of diffusion for some small volume gives a relation including a "sink form ($\alpha\phi$)" as follows:

$$\dot{\phi}/\dot{t} = D\ddot{\phi}/\ddot{x} - \alpha\phi \tag{2.2}$$

Here ϕ is the concentration of the vapor. D is the diffusivity. Because the deposition time is long enough, the concentration profile should be time independent. Without the boundary conditions, the solution to the differential above is:

$$\phi = A\exp(\beta z) + B\exp(-\beta z) \tag{2.3}$$

Here β is $\sqrt{\alpha/D}$. With the boundary conditions:

$$\phi_{z=0} = \phi_0 \tag{2.4}$$

$$\dot{\phi}_{z=h}/\dot{z} = 0 \tag{2.5}$$

Here ϕ_0 is the vapor concentration at z=0, and the corrected vapor concentration distribution is:

$$\phi = \phi_0(\exp(\beta z) + \exp(2\beta h - \beta z))/(1 + \exp(2\beta h)) \tag{2.6}$$

If the vapor concentration is dominant in the diameter of the Si/CNTs, the Si/CNT diameter should be proportional to the vapor concentration and infiltration time. To verify the effect of the concentration variance on the infiltration process, we choose a diffusivity and time a proportional coefficient to the equation (2.6). A comparison between the adjusted result and the Si/CNT diameters is shown in Fig. (2.10), in which the red line is the modeling result and the blue dots are Si/CNT diameters measured by the SEM.

The modeling result fits well to the experimental measurement, however, there is a mismatch at the bottom of the forest. The mismatch may result from the temperature gradient from the top to the bottom of the forest. Although the temperature difference between the top and the bottom of the forest is small, the diffusivity varies in most systems as an
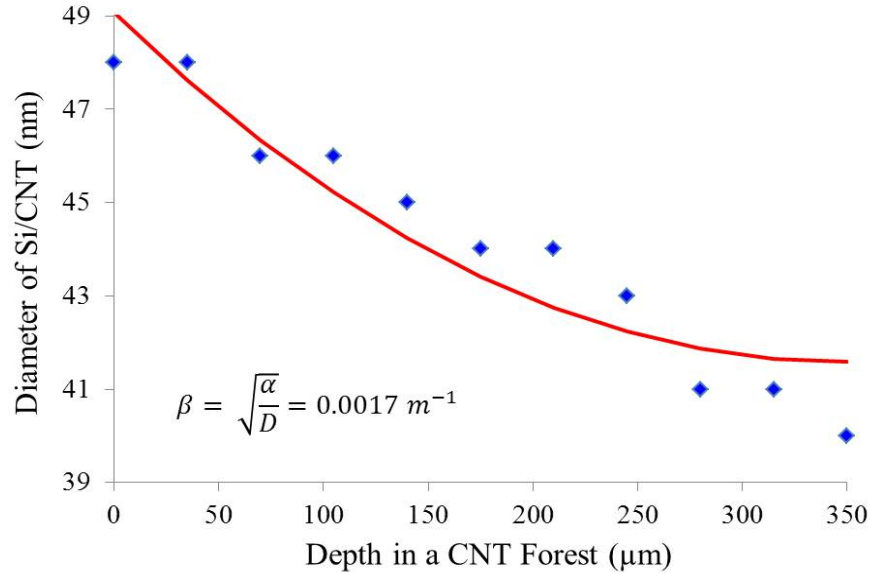
Figure 2.10 Trendlines of the diameter os Si/CNTs by a SEM measurement (blue dots) and a theoretical model (red line)

exponential function of temperature. As a result, the weak temperature gradient affects obviously on the concentration. Concluded from Fig. (2.10), the concentration variance is more dominant in Si/CNT diameter variance than the other infiltration process parameters including pressure and vapor flow rate. As a result, if we expect to improving the Si/CNT diameter uniformity, the concentration difference between the top and the bottom of a CNT forest should be minimized.

2.6 Discussion and Conclusion

The data shown for Raman, EELS and imaging results are consistent with the proposed pictures of carbon nanotubes coated with amorphous or poly-crystalline silicon. The coating rate is weakly dependent on depth, and the rate should also depend on the CNT pattern as well as the parameters of the LPCVD process. To achieve uniform Si/CNT diameters, the

deposition rate must be limited by the kinetics of surface growth rather than the transport of gases to and from the CNT surface. Patterning gas access holes have previously been shown to improve gas transport and silicon infiltration uniformity,[65] which is agreed with our theoretical study because gas holes contribute to the vapor concentration uniform distribution in the CNT forest. To improve the uniformity of silicon coatings on CNTs, temperature can be helpful since diffusivity (D) is dependent on temperature. We have seen some evidence that lower LPCVD temperatures coat more slowly but more uniformly. The average spacing between CNTs in this process is $\sim$ 100-150 nm, thus limiting Si/CNT diameters to $\sim$ 200 nm at which point the structure is mostly filled.

Silicon deposition on the CNTs typically forms a conformal coating but occasionally results in separated beads along the CNTs, as seen in Fig. (2.8)b and Fig. (2.6)a. This bead formation may be due to insufficient coating, a smaller diameter of the underlying nanotube or a combination of these factors. In general, droplet or bead formation on a fiber depends upon the atoms having sufficient mobility to form the energetically preferred structure, the relative surface energies, on the diameter of the fiber.[66] In our CNT growth process, multi-walled CNTs were formed with a distribution of tube diameters (averaging 8 to 10 nm in diameter). We suggest that at the Si deposition temperature ($>$ 500 °C) silicon atoms have sufficient mobility to form beads of silicon on the multi-walled CNTs. Those initially formed beads then grow and combine to form conformal coatings. The specifics of that bead-to-conformal coating process will depend upon the individual CNT diameter, the deposition temperature, and the amount of silicon on the CNT. In Fig. (2.8) we estimate that at 530 °C our typical CNT (8 to 10 nm in diameter) is conformally coated after approximately 15 nm of deposition ($\sim$ 40 nm total diameter including the CNT).

In conclusion, vertically aligned and patterned silicon-carbon core shell nanotubes have been synthesized by the CNT-M process. These Si/CNTs are uniform in morphology con-

sisting of a multi-walled nanotube core and an amorphous or crystalline silicon shell. No evidence of a SiC layer at the interface was seen by Raman or EELS.

Chapter 3

Carbon Nanotube Templated Microfabrication of Porous Silicon-Oxide Nanowires with an Application to Chemical Separations

3.1 Introduction

Several functional properties of materials are impacted by the three dimensional shape of the material on both the micrometer scale (microscale) and nanometer scale (nanoscale). Microscale patterning of a material affects several functional properties including fluid flow, ion and electron conductivity, mechanical response, and interactions with electromagnetic fields and waves.[67,68] Nanoscale structuring can dramatically change chemical reaction rates and surface adsorption capacity as the surface to volume ratio significantly increases.[69] Electronic materials properties including band structure, recombination rates, and mobilities are

strongly influenced by nanoscale structuring.[70] Often multiple physical properties are coupled and are jointly influenced by nanoscale structuring as is the case for strained silicon: nanoscale strain control is used to produce higher mobilities than achievable in the bulk.[71] Coupling between strain and electrochemical properties was observed in nanoscale silicon particles deposited on carbon nanotubes which resulted in improved electrochemical cycling over bulk silicon anodes for lithium ion batteries.[72]

Since both micro and nanoscale structuring influences functional material properties, the ability to control microscale shape in a variety of nanostructured materials will enable a wide range of applications. Precise three dimensional microscale structures have been widely fabricated by reactive ion etching (RIE) wherein bulk semiconductor, metal, and ceramic materials are micromachined into the desired shapes.[73] Deep reactive ion etching has resulted in high aspect ratio structures in silicon.[74] High aspect ratio structures with vertical sidewalls were also fabricated by using vertically aligned carbon nanotube grown from micropatterned catalyst layers.[75,76] However, the as-grown nanotube density is low and the tubes are held to each other only by weak van der Waals forces resulting in structures that are too weak to maintain their microscale shape when put in contact with fluids. Recently, templated microfabrication of robust high aspect ratio structures in silicon, silicon nitride, and carbon has been done using carbon nanotube (CNT) frameworks.[65] On the nanoscale, silicon materials including silicon nanowires (SiNWs), silicon nanotubes (SiNTs), and porous silicon have previously been fabricated by a variety of methods including chemical vapor deposition, template-assisted growth, solution phase synthesis, and electrochemical etching. Vertically etched porous silicon has been used to produce microscale features with vertical nano-pores by masking and plasma etching. Carbon nanotubes also have been used as a nanoscale template for various materials, including polymers,[77] metal,[78] metal alloy,[79,80] and silicon.[51,81–83] While these prior methods have been used to fabricate structures on the nano

and microscale there has not been a general, flexible method for three dimensional patterning that spans the entire range from nano to micro.

3.2 Fabrication of Porous Silicon-Oxide Nanowires

Here we introduce a fabrication process that results in control over length scales, ranging from several nanometers to several hundred microns. The process, called carbon nanotube templated microfabrication (CNT-M) uses partial Si infiltration of carbon nanotube frameworks to fabricate porous three dimensional microscale shapes consisting of silicon-carbon core-shell nanotubes (Si/CNTs) as illustrated in Fig. (3.1)a-c. The addition of thin silicon shells to the vertically aligned CNTs (VACNTs) enables the fabrication of robust silicon nanostructures with the flexibility to design a wide range of geometries by CNT-M. Fig. (3.1) illustrates the hierarchical nature of the geometry and the ability to control geometric dimensions over a broad range of length scales.

We illustrate the utility of this hierarchical structuring approach by fabricating micropatterned plates for a chemical separation technique, high resolution thin layer chromatography (TLC). In TLC, samples are spotted near the bottom of a plate and carried up the plate by solvent fluid flow by capillary action. If the solvent (mobile phase) and materials in the TLC plate, i.e., stationary phase, are chosen correctly, different analytes move up the plate at different speeds resulting in separated spots when multiple analytes are present. In TLC, the separation mechanism results from different equilibrium constants of analytes partitioning themselves between the mobile and stationary phases. Spatial non-uniformity in fluid flow spreads each TLC analyte spot, resulting in low resolution. Consequently, high resolution separations require control of structure on the microscale for uniform solvent flow.[55] High resolution TLC (at practical concentrations) requires a nanostructured, high area surface to keep the surface from overloading with analyte and consequently spreading the analyte spot.

Patterned SiCNT Dimensions		
	Minimum	Maximum
Pattern (P)	0.5 um	10 cm
Height (H)	10 um	1 mm
Diameter (D)	10 nm	120 nm
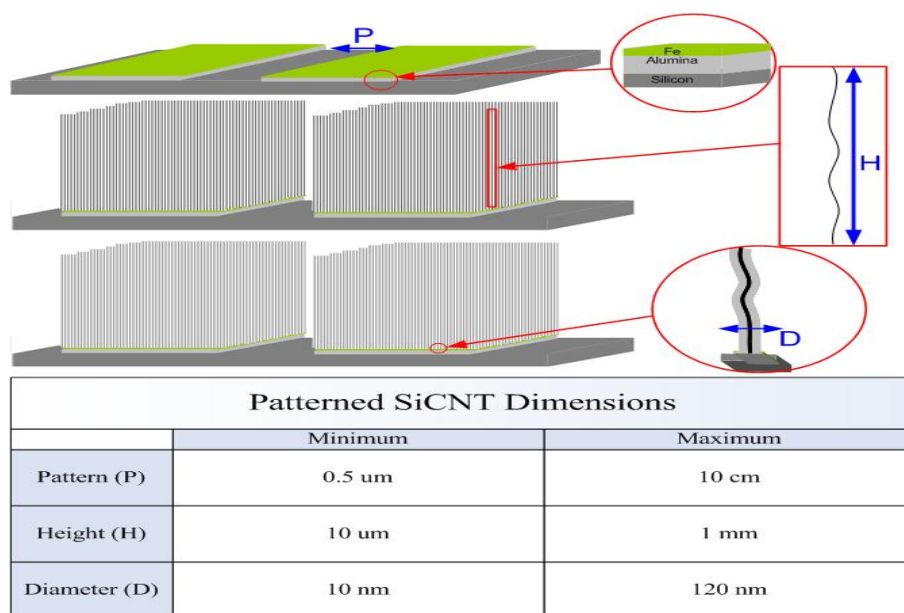
Figure 3.1 Patterning 3D structures with control over a hierarchical set of length scales. (a-c) Diagram of the fabrication process for patterned Si/CNTs using a vertical CNT template. (a) Photolithography, deposition and a lift-off process yields a two dimensional (2D) alumina and iron catalyst layer. (b) CNTs grow vertically from the patterned catalyst and form a three dimensional (3D) structure. (c) Si/CNTs are formed by coating the CNTs with Si by LPCVD. (d) The fabrication dimensions can be controlled over several length scales as outlined in the table, and limited only by the lithography system

Commercial TLC plates are fabricated by coating glass or metal surfaces with porous silica microparticles. The microparticles are deposited on the surface under carefully controlled processes and held together with a binder (e.g., gypsum or polyvinyl alcohol). Although commercial TLC is a mature technology there is significant room for improvement in microstructure regularity when compared to lithographically defined structures. Structures have previously been microfabricated for chromatography but the lack of nanoscale porosity severely limits the capacity of these structures.[84] Here we have constructed binder-free TLC plates using an extension of the CNT-M process. The extension adds a thermal oxidation step after Si infiltration; the oxidation step converts the Si to silica and removes the carbon nanotubes. TLC was performed on the resulting silica plates, showing improvement over commercial high performance TLC (HPTLC) plates.

Vertically-aligned CNT forests were grown from a patterned iron catalyst layer on a silicon substrate by thermal chemical vapor deposition (CVD) methods. Briefly, the silicon substrate was patterned by photolithography and lift-off of a catalyst stack consisting of 30 nm of Al_2O_3 and 3 nm of Fe. The substrate was placed in a 1" tube furnace and the temperature was ramped to 750 °C over 10 mins in hydrogen (400 sccm). When the furnace reached 750 °C, the CNTs were grown by flowing ethylene (700 sccm) and hydrogen (400 sccm). Following growth, cooling was done under Argon (250 sccm). The CNTs were then put into a 16 cm diameter tube in a low pressure chemical vapor deposition (LPCVD) reactor. Amorphous silicon films were deposited onto the nanotubes from silane (20 sccm) at 530 °C and at 150 mtorr.

The Si/CNTs were then annealed in air at 1000 °C for 5 hrs to oxidize the silicon and to combust the cabon nanotubes. The Si/CNT structures used for the oxidation process had continuous silicon rather than the beadlike morphology. This is because the samples for oxidation started as shorter, patterned CNT structures that were coated with silicon

for a longer time, resulting in thicker silicon layers and a core-shell tube morphology. The silica nanowires are then subjected to a hydrating step to increase the silanol content on the surface. The hydrating process employed a 0.1 M HCl: methanol (1:1) solution that was heated overnight at reflux temperatures and methanol is used to aid in wetting the surface. After the hydration process the material was rinsed thoroughly with water to remove any residual acid and was dried at 110 °C.
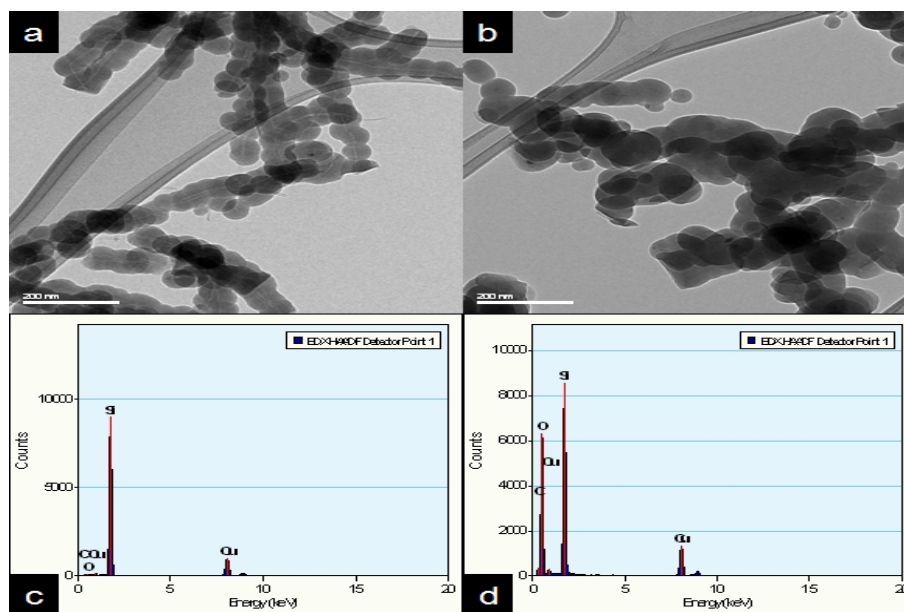
Figure 3.2 TEM images of Si/CNTs before oxidization (a) and after oxidization (b) are shown; EDAX spectra of Si/CNTs before oxidization (c) and after oxidization (d) are shown

In addition to the CNT-M plate, a Merck TLC plate (250 μm thick sorbent layer) and a Merck HPTLC plate (150 μm thick sorbent layer) were used for comparison. The TLC plates were used to separate a CAMAG (Muttenz, Switzerland) test dye solution that was dissolved in hexanes (3% v/v). A 0.5 μL aliquot of the diluted test dye mixture was spotted 5 mm from the bottom of the plate. Toluene was used as the mobile phase. A twin trough chamber (CAMAG, Muttenz, Switzerland) was equilibrated with 3 mL of toluene for 10 minutes prior to chromatography. The TLC plates were developed over a 45 mm length

with 3 mL of toluene. The resulting developed TLC plates were digitized using a flat-bed scanner (600 × 600 dpi., MX-2300N, Sharp, Romeovill, IL).

3.3 Application of Nanowires in Thin Layer Chromatography

We applied the CNT-M process to fabricate plates for thin-layer chromatography (TLC). The Si/CNTs were grown in a herringbone pattern as shown in Fig. (3.3)a,b. The resulting pattern has the right microscale shape for TLC: open channels for rapid fluid flow and thin porous walls for rapid analyte diffusion and interaction. The high nanoscale porosity and corresponding high surface area are also important for high analyte capacity. A significant problem, however, is that the Si/CNT forest is optically dark whereas TLC plates are typically white for easy visualization of the analyte spots. To reduce optical absorption, the Si/CNT structure was annealed in air to convert the silicon to silica and oxidize the CNTs as shown in Fig. (3.2). The 3D herringbone pattern was preserved through the oxidation step and the samples are optically white. The high temperature oxidization process did cause volume expansion resulting in the features becoming wider. In our TLC experiments, we used mask designs that compensated for this expansion. TEM analysis of the oxidized materials confirmed that the silicon was converted to silicon oxide and that the CNTs were removed. SEM images of the chromatographic material are shown in figure 3d along with a demonstration of TLC plate performance in separating a series of dyes.

The CNT-M plate performance was compared with commercial TLC and HPTLC plates as shown in Fig. (3.4). The comparison was quantitative by two figures of merit: TLC efficiency and retention factor. The efficiency (number of theoretical plates, N) and retention factor (R_f) for each analyte have been calculated for CTN-M TLC, commercial HPTLC, and
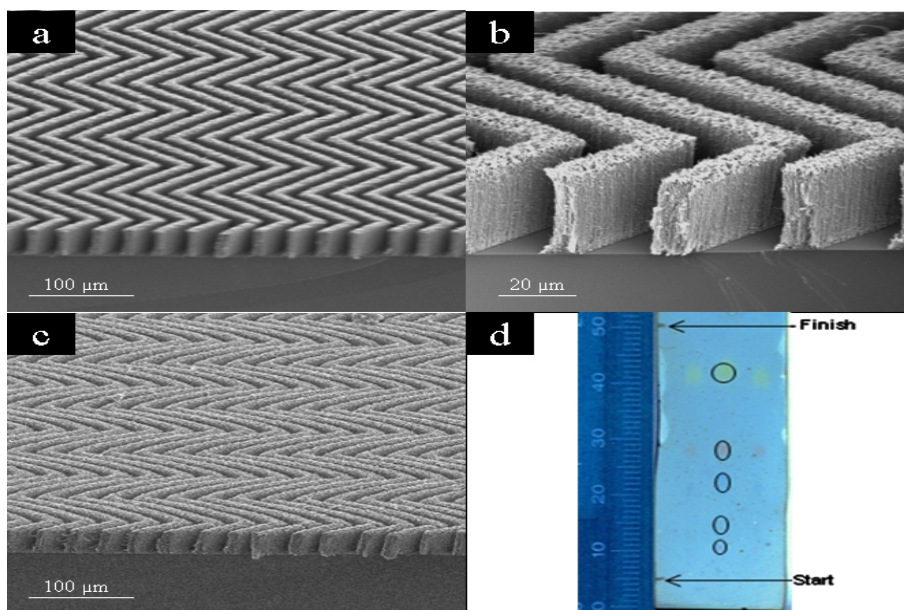
Figure 3.3 Si/CNTs based chromatography plates. (a,b) Herringbone CNT pattern was partially infiltrated with silicon for 80 minutes resulting in 4 micron hedges and 7 micron spaces. (c) Herringbone pattern after annealing at 1000 °C for 5 hours in air for oxidation of the silicon and the nanotubes. The resulting structure consists entirely of SiO_2 nanowires. (d) Separation of a CAMAG dye test mixture

commercial TLC plates and are tabulated in Fig. (3.5). The efficiency was calculated by equation (3.1), where z is the distance the analyte traveled, l is the distance the solvent front traveled (migration distance), and w is the chromatographic width of the analyte in the direction of the solvent front.

$$N = 16zl/w^2 \tag{3.1}$$

a. The microfabricated TLC plate.
Mobile phase: Toluene
Dye concentration: CAMAG in Hexanes
(3 % v/v)
Migration distance 45 mm
Developing time: 4.5 minutes
Thickness of sorbent layer: 50 mciron

b. A commercial TLC plate.
Mobile phase: Toluene
Dye concentration: CAMAG in Hexanes
(3 % v/v)
Migration distance 45 mm
Developing time: 4 minutes
Thickness of sorbent layer: 250 micron

c. A commercial HPTLC plate
Mobile phase: Toluene
Dye concentration: CAMAG in Hexanes
(3% v/v)
Migration distance: 62 mm
Developing time: 12 minutes
Thickness of sorbent layer: 150 micron

Figure 3.4 The images of the CNT-M plate (a) and two commercial plates (b and c) after the separation were compared. z is the distance the analyte traveled, l is the distance the solvent front traveled (migration distance), and w is the chromatographic width of the analyte in the direction of the solvent front

The retention factor was calculated by equation (3.2), where z is the distance the analyte traveled and l is the distance the solvent front traveled.

$$R_f = z/l \tag{3.2}$$
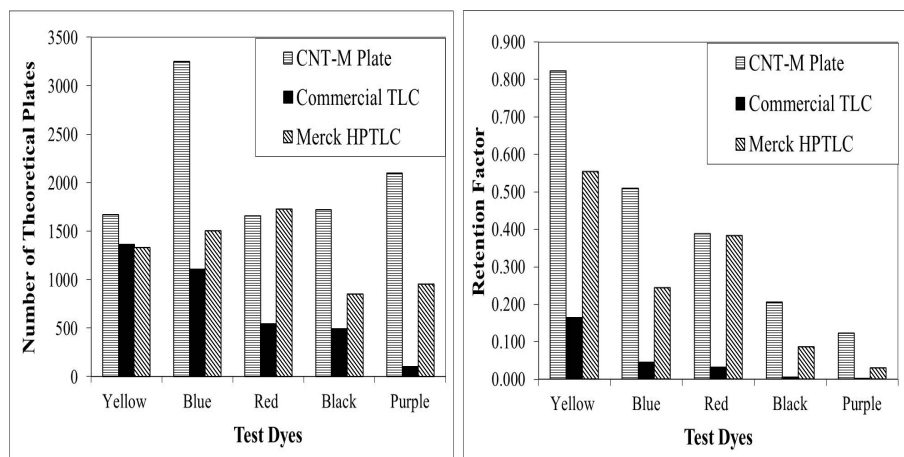
Figure 3.5 The efficiency (number of theoretical plates, N) and retention factor (R_f) for each analyte are compared between CNT-M TLC, TLC, and HPTLC plates. (The colors in x-axis from yellow to purple represent different analytes in dyes.)

3.4 Analysis of Thin Layer Chromatography

These 3D patterned silica structures demonstrate chromatographic efficiencies that either equal or exceed those of HPTLC and exceed those of commercial TLC plate. In addition to the increased efficiencies that have been demonstrated there was also an improvement in the speed of the separation. To analyze the features that allow CNT-M plates to outperform commercial plates, we refer to the van Deemter equation ((3.3)) for plate height (H).

$$H = A + B/v + C \cdot v \tag{3.3}$$

A smaller plate height will result in a larger number of plates and a corresponding higher efficiency. The first term in the equation, the A term, is the eddy diffusion term and is caused by differences in fluid path length taken by different solute molecules. In microstructured media these path length differences result from inhomogeneities in the microscale structures, which for us are minimized due to the precisely controlled microscale patterns of CNT-M plates. The contribution from the second term, the B term, relates to longitudinal diffusion

and is reduced at higher flow velocities. The CNT-M plates had much shorter development times corresponding to higher velocities and therefore a reduction in the diffusion term contribution is expected. These higher velocities were possible because the CNT-M structures could be fabricated with wider, more direct flow channels than particulate media. The last term, the C term, comes from the mass transfer kinetics of the analyte between mobile and stationary phases and is reduced by decreasing particle size, or in our case hedge width. Our hedge width is nominally 4 μm wide for the CNT-M plates analyzed. This is smaller than the particle sizes of both of the commercial plates. The commercial TLC plates had particles with diameters ranging from 5-20 μm and the HPTLC plates had particles ranging from 6-8 μm. Therefore the C term should also be significantly lower than C term of commercial TLC plates and slightly lower than C term of HPTLC plates. Since this term is multiplied by the velocity v, there may not be an improvement in this term as CNT-M velocities are higher. Additionally the ability to controllably adjust the microscale geometry with CNT-M should provide an ideal test bed for future quantitative studies of the contribution of each of these terms to efficiency.

Since the solute travels different distances between the inner corner and outer corner of the hedge shown in Fig. (3.6), so solute spreading can delay the mobile phase transport.

Moreover, the effect can be quantified by comparing the spreading width and the hedge length as following:

$$L = 2a/(\tan\theta/2) \tag{3.4}$$

Here a is the perpendicular distance between two hedges, θ is the corner angle of the hedge, and L is the mobile phase traveling difference between inner lane and outer lane when it passed through the corner. In our plate, a is 7 μm and is 90°, so L is 14 μm.
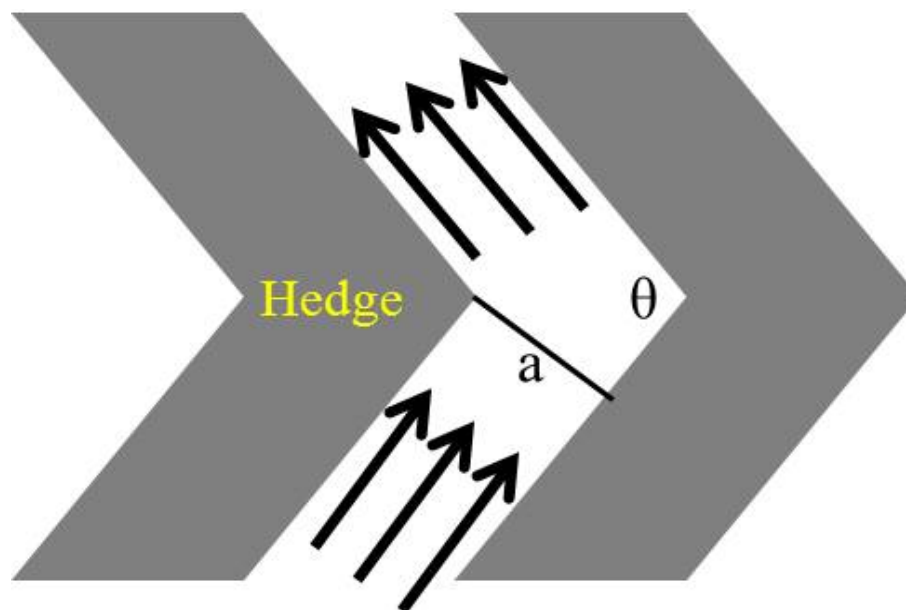
Figure 3.6 A sketch of mobile phase transferring through the zigzag pattern

$$t = L/u \tag{3.5}$$

t is time spent by solute molecules in the mobile phase, and u is the average mobile phase velocity. In our case, u is about 400 μm/s. The spreading of a zone due to molecular diffusion in the mobile phase can be calculated from the Einstein equation:

$$\sigma = \sqrt[2]{2Dt} \tag{3.6}$$

Here D is a diffusion coefficient of a solute, approximately 1000 μm^2/s. As a result, the spreading width σ is 8.4 μm.

The mobile phase transport can be influenced by the fluid spreading along the fluid flowing direction. The fluid spreading h can be gained by a geometry conclusion as shown in Fig. (3.7). Compared with the length of hedge (100 μm), the fluid spreading is large so the solute spreading can influence on the mobile phase transport.
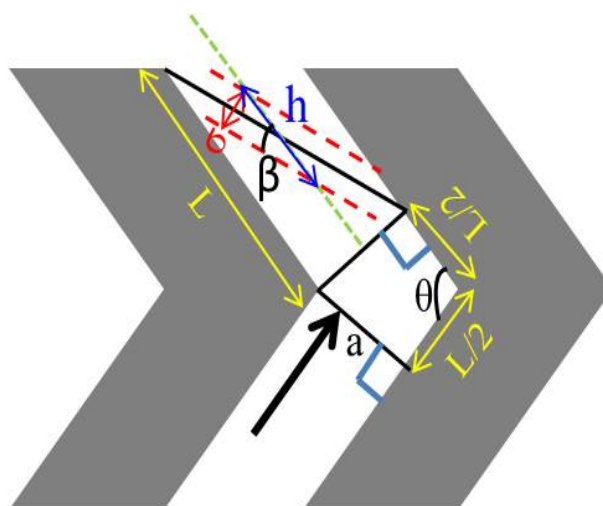
$$h = \frac{\sigma}{\sin(\beta)} = \frac{\sqrt{2D\dfrac{2a}{u\cdot\tan\dfrac{\theta}{2}}\sqrt{a^2+L^2}}}{a} = 2\sqrt{\frac{D}{u\cdot\tan\dfrac{\theta}{2}}\cdot(1+\frac{4}{(\tan\dfrac{\theta}{2})^2})} = 18.8\ \mu m$$

Figure 3.7 A sketch of mobile phase transferring through the zigzag pattern

3.5   Conclusion

Using the CNT-M process, we were able to fabricate porous Si/CNT and silica structures with control over 3D microscale shape and nanoscale porosity. We view these 3-D porous structures as powerful testbeds for studying a variety of micro and nanostructured materials properties as well as chemical and physical processes on the micro and nanoscale. Furthermore, these hierarchical structures appear promising in applications including chemical separations, catalysis, energy storage, and energy conversion. We applied the CNT-M process to fabricate silica plates for TLC that outperformed commercial HPTLC plates. It should be possible to extend the CNT-M process to microfluidics, high performance liquid chromatography (HPLC) and ultra high performance liquid chromatography (UPLC).

Chapter 4

High Capacity Carbon Nanotube Templated Silicon Anodes for Lithium Ion Batteries

4.1 Introduction

Silicon is a promising candidate anode material for lithium ion batteries due to its high theoretical capacity (4000 mAh/g).[41,42] However, volume changes during the insertion and extraction of lithium cause pulverization of bulk silicon resulting in failure of the electrode after very few cycles.[42,85] Nanostructured silicon including silicon nanoparticles,[45] nanowires and nanotubes[21,47,86] has been used to make electrodes with specific capacities over 3000 mAh/g (10 times higher than commercial carbon anodes) and improved cycle life relative to bulk silicon. Research on nanostructured silicon as an electrode material has recently accelerated with investigation of the influence of diameter,[49] doping,[87] carbon coating,[47,86] and solid electrolyte interphase (SEI) layer stability[88–91] on electrochemical performance. A

significant hurdle is maintaining electrical and ionic conductivity in these materials during the considerable volume changes that occur upon cycling.[90–92] Carbon nanofibers (CNFs) and carbon nanotubes (CNTs) have been used as templates to form silicon-carbon nanocomposites by depositing silicon onto the nanostructured carbon.[51–53,93]

Although research on nanostructured silicon anodes has resulted in materials with extremely high specific capacities, it has not generally resulted in materials with correspondingly high areal and volumetric capacity. High areal and volumetric capacities are critical for realizing high capacity batteries as the anode is only one of several contributors to the battery mass and volume. In Li-ion batteries, the active materials typically contribute less than half of the total battery mass.[94] Other contributions to the mass scale with the electrode area (superficial) and, in the case of electrolyte mass, the pore volume of the electrode. Silicon areal capacities (capacity per "top down" or superficial area) have generally been quite low for nanostructured electrodes,[21] although areal capacities slightly higher (4 mAh/cm^2) than that of commercial carbon anodes (~ 3 mAh/cm^2)[94] have been demonstrated.[15,94] Volumetric capacities have been very high in thin film silicon anodes (9320 mAh/cm^3), but these thin silicon films yield very low areal capacities.[95] Recently, Hu et al. reported much higher areal capacities of 40 mAh/cm^2 that were achieved with the use of a Si-CNT "sponge."[21] Although promising, this approach resulted in a small volumetric silicon loading and correspondingly low volumetric capacity.[96]

We report here the synthesis of Si/CNT composites by deposition of silicon onto vertically aligned CNT (VACNT) templates. VACNT templates eliminate the need for a polymer binder in electrode fabrication and facilitate the desired lithium ion and electron transport in the electrode.[17] In this study we take advantage of the precise control of electrode geometry made possible by such templates to investigate a wide range of silicon loadings by varying both the silicon to carbon nanotube (Si:CNT) mass ratio and the electrode thickness. The

Si:CNT mass ratio was varied from 9:1 to over 80:1, and electrode thickness was varied from 7 μm to 40 μm. Stable cycling was observed for electrodes with Si:CNT mass ratios up to 50:1; electrodes with mass ratios higher than this were observed to fade at a significantly more rapid rate. A Si:C mass ratio of close to 50:1 yielded areal capacities over 9 mAh/cm^2, (3 times the value for commercial carbon anodes), volumetric capacities over 4600 mAh/cm^3 (20 times the value for commercial carbon anodes), and a specific capacity of 2700 mAh/g.

4.2 Fabrication of Silicon-Carbon Nanotube Composites

VACNT templated synthesis of nanostructured silicon allows control of structural parameters over a wide range; these parameters include the thickness of the composite layer, the silicon to CNT (Si:CNT) mass ratio, and the silicon microstructure. A sketch of the silicon-carbon nanotube (Si/CNT) composite structure is illustrated in Fig. (4.1)a. Experimental details on the fabrication of the composite electrodes are described in the supplementary information. Briefly, vertically aligned multi-walled carbon nanotubes (MWCNTs) were grown on stainless steel substrates with the aid of a catalyst layer. The catalyst layer consisted of a bilayer of 4 nm of iron on a 30 nm thick alumina barrier layer. Silicon infiltration of the carbon nanotube framework with LPCVD resulted in robust, porous Si/CNT composites consisting of silicon shells surrounding individual CNTs. The porosity of the nanocomposites (and correspondingly, the Si:CNT mass ratio) is dependent on the silicon infiltration process parameters and the infiltration time. Fig. (4.1)b-h show SEM and TEM images of the Si/CNT composites. As seen in Fig. (4.1)b and (4.1)e, the composites retain the vertical orientation of the pristine CNT forest. The different thicknesses of the composites are the result of different CNT forest heights, which are controlled by varying the run time for

carbon nanotube growth. The CNT growth rate is nearly constant for short growth times. For example, 21 seconds results in a CNT forest with an average height of 9 ± 2 μm, and 75 seconds results in a CNT forest with an average height of 27 ± 5 μm.
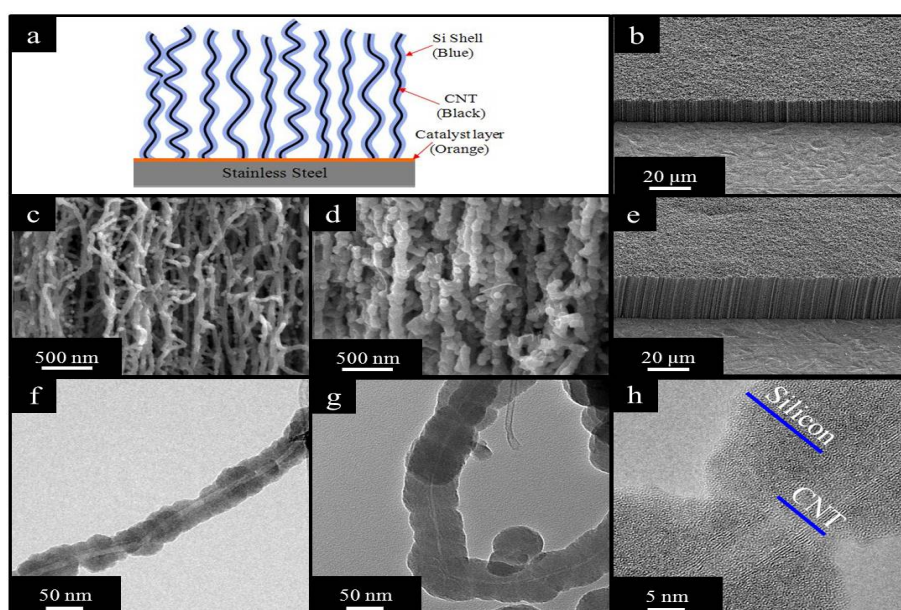
Figure 4.1 (a) A diagram of a VACNT templated silicon electrode (Si/CNT composites) is shown. All materials have been labeled in the sketch but the dimensions of the materials are not to scale; (b) An SEM image of a ~ 12 μm thick Si/CNT composite electrode on the stainless steel foil is shown; (c,d) SEM profile views of the Si/CNT composite with thin (c) and thick (d) silicon shells are shown; (e) An SEM image of a ~ 27 μm thick Si/CNT composite electrode on the stainless steel foil is shown; (f,g) TEM images of silicon coated CNTs with 16 nm (f) and 36 nm (g) silicon shells are shown; (h) A TEM image of an individual silicon coated CNT is shown; the CNT and amorphous silicon are labeled

The average diameter of MWCNTs synthesized in our experiment (~ 12 nm) is significantly less than the average space between nanotubes (~ 100 nm); consequently, the silicon shell thickness can be varied over a large range. These silicon shells are quite uniform on VACNT samples up to 50 microns high.[93] The thickness of the silicon shell coating was 14 ± 3

nm for a 40 min silicon infiltration, 25±5 nm for 60 min infiltration, and 35±5 nm for an 80 min infiltration. Fig. (4.1)c and (4.1)d are close-up views of nanotubes with thinner ($\sim$ 16 nm) and thicker ($\sim$ 36 nm) silicon shells, respectively. As seen in the image, the structure of the Si/CNT material is generally vertical, but with individual tubes following an undulating path. TEM images of individual nanotubes coated with silicon for different times are shown in Fig. (4.1)f (40 min coating) and Fig. (4.1)g (80 min coating) resulting in $\sim$ 44 nm and $\sim$ 84 nm diameter structures respectively. Varying the silicon coating time resulted in Si:CNT mass ratios from 9:1 to 80:1, as determined from SEM measured diameters of the tubes before and after coating. The mass ratios were calculated from these diameters using the following expression:

$$Mass\,ratio = \rho_{Si} \times (r^2_{Si/CNT} - r^2_{CNT})/(\rho_{CNT} \times (r^2_{CNT})) \tag{4.1}$$

Here d the expected density of the amorphous silicon (1.9 g/cm^3), $r_{Si/CNT}$ is the radius of Si/CNTs, r_{CNT} is the radius of CNTs, and is the expected density of mutilwalled carbon nanotubes (1.5 g/cm^3). The high resolution micrograph in Fig. (4.1)h shows the morphology of a silicon coated CNT in which the silicon and CNT locations are labeled. In our work, low deposition temperatures (500 - 550 °C) were used to provide uniform deposits. These low temperatures also yield amorphous silicon layers, which exhibit much smaller first cycle capacity losses than crystalline silicon films.[97]

The nanocomposite electrodes were tested in battery cells consisting of the electrode of interest, the electrolyte, and a lithium metal counter electrode. A Celgard separator was used for the tests. Because of the sensitivity of the cell components to water and oxygen, cells were assembled in an argon-filled glove box (moisture content 0.9 ppm and oxygen content < 0.25 ppm, VAC, Hawthorne, CA) and packaged for testing outside of the box. A standard electrolyte mixture of EC and DEC containing 1M LiPF$_6$ was used. The tests

were performed with use of a MACCOR system (Maccor 4300, Maccor Inc.). In this work, we refer to lithium insertion into silicon (alloying) as charging, and lithium extraction from silicon (de-alloying) as discharging. All cells were cycled between 1.0 and 0.02 V. Reported C rates assume an electrode capacity of 2.5 hr/g, as is common practice for silicon electrodes.[51] For example for 1C, the current is chosen such that I = capacity(2.5 A/g) × silicon mass.

4.3 Electrochemical Performance of Si/CNT Composites

Electrochemical testing of our Si/CNT composite is shown in Fig. (4.2). The voltage profile, including the slope changes at at 0.3 V and at 0.1 V during the first charging cycle, is consistent with the previous studies of nanostructured amorphous silicon.[95] In the first cycle, the observed charge capacity was 3000 mAh/g and discharge capacity was 2118 mAh/g, corresponding to a columbic efficiency of 71 %. A drop in capacity was observed in the third cycle due to an increase in the C-rate (from 0.4C to 0.8C), followed by a slight increase in capacity starting with the fourth cycle. A stable capacity of $\sim$ 2050 mAh/g at 0.8C was observed for 20 cycles, with a coulombic efficiency of

$$\sim$$

93 %. The specific capacity of these electrodes at this C rate is significantly higher than that observed for silicon/carbon composite electrodes reported previously in the literature.

Experiments were performed to determine the impact of composite thickness and silicon shell thickness (silicon loading) on the specific capacity. The results shown in Fig. (4.3) represent the charge capacity of the 4th cycle at a C/4 rate. No significant decrease in capacity as the thickness increased from 6.9 to 30 microns was observed (Fig. (4.3)a). Similarly, no
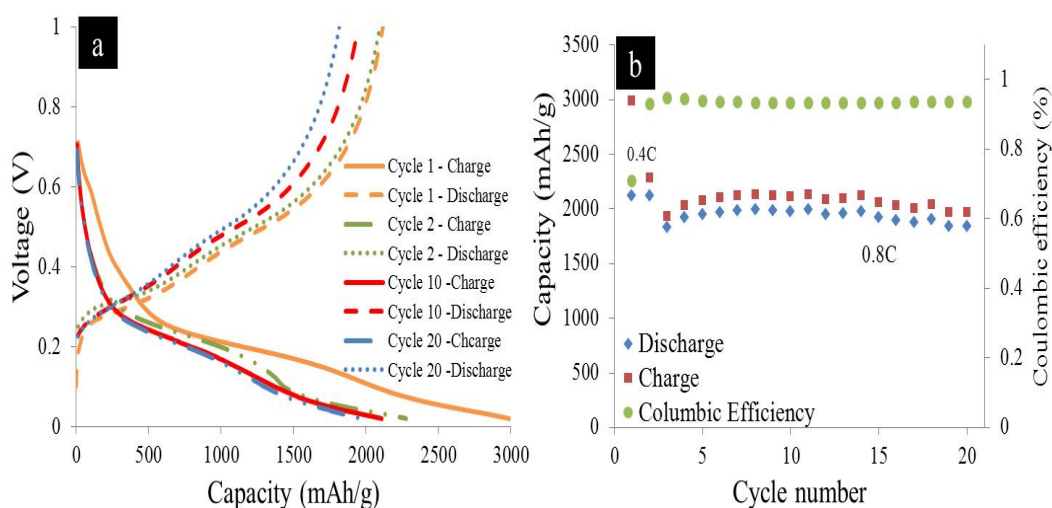
Figure 4.2 Electrochemical performance of Si/CNT composite electrodes with a thickness 6.5 μm and a Si:CNT mass ratio 17:1. (a) Voltage profile of Si/CNT composites; (b) Charge (square) and discharge (diamond) capacity and Columbic efficiency (round) versus cycle number for the Si/CNT composite electrode at 0.8 C (two 0.4 C conditioning cycles were done first)

significant decrease in capacity was observed as a function of Si:CNT mass ratio for mass ratios that ranged from 9:1 to 79:1 (Fig. (4.3)b). In contrast, a similar comparison at a higher rate of C/2 indicated a dependence of the capacity on loading, with higher silicon loadings showing lower capacities. Specifically, the capacities at Si:CNT mass ratios of 15:1 and 65:1 were $\sim$ 1900 and $\sim$ 1500 mAh/g, respectively.

The stability of the capacity upon repeated charge and discharge cycling is strongly dependent on the silicon loading as summarized in Fig. (4.4). For low silicon loading, the cycle stability was good for all composite layer thicknesses tested (figure Fig. (4.4)a). In contrast, highly loaded samples (Si:CNT above 60:1) did not cycle well for the same range of layer thicknesses (Fig. (4.4)b). A summary of capacity stability at different silicon loadings is shown in Fig. (4.4)c where samples with capacity fading less than 20 % in 20 cycles are classified as good. The fraction of samples with good cycle stability was 0.95 when Si:CNT
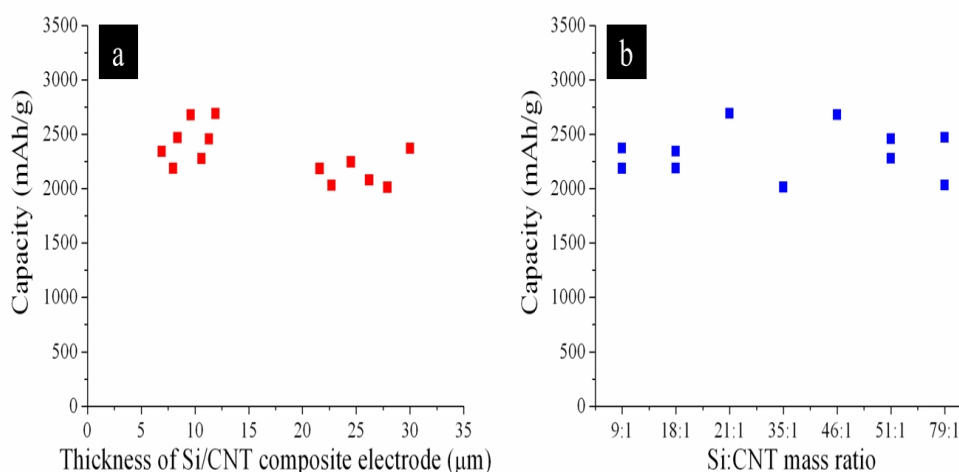
Figure 4.3 The 4th cycle charge capacities of 13 samples with varying heights (from 6.9 μm to 30 μm) and varying Si to CNT mass ratios (from 9:1 to 79:1) at a rate of C/4 as a function of (a) electrode thickness and (b) mass ratio

ratios were below 60, but 0.05 when ratios were above 60.

A high areal capacity with good capacity stability is achieved in electrodes $\sim$ 20 microns thick with Si to CNT mass ratios of approximately 50:1. Fig. (4.5) shows an electrode consisting of a composite layer 19.4 μm thick with a Si:CNT mass ratio of 51:1 and an areal capacity of $\sim$ 9 mAh/cm^2. This is three times the areal capacity of commercial graphite lithium ion battery anodes ($\sim$ 3 mAh/cm^2),[94] which is shown by the dashed line in Fig. (4.5) for comparison. The volumetric capacity of the electrode was $\sim$ 4600 mAh/cm^3, which is about 20 times that of commercial lithium ion battery anodes ($\sim$ 230 mAh/cm^3). After 20 cycles, the capacity loss was $\sim$ 12 % of the initial capacity.

Fig. (4.6) shows charge and discharge capacity observed at rates of C/10, C/5, C/2, and 1C. At each C-rate, the cell was tested for 4 cycles to ensure the reliability of the capacity data. The observed capacities per mass were approximately 3000, 2570, 1890, and 1440 mAh/g, respectively. The capacity decreased significantly with increasing C-rate as shown
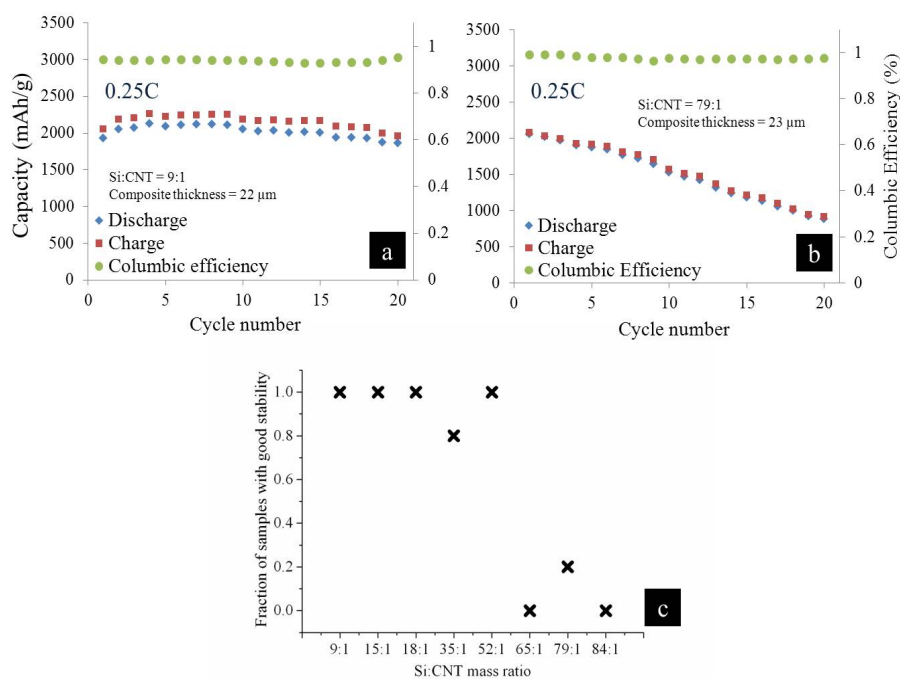
Figure 4.4 The influence of composite layer thickness and Si loading on cycle stability: (a) sample with a strong cycle stability, (b) sample with a weak cycle stability, and (c) summary of cycle stability results for different Si/CNT mass ratios. Each data point in (c) represents an average of multiple samples; data from each sample is given in the supplementary information.
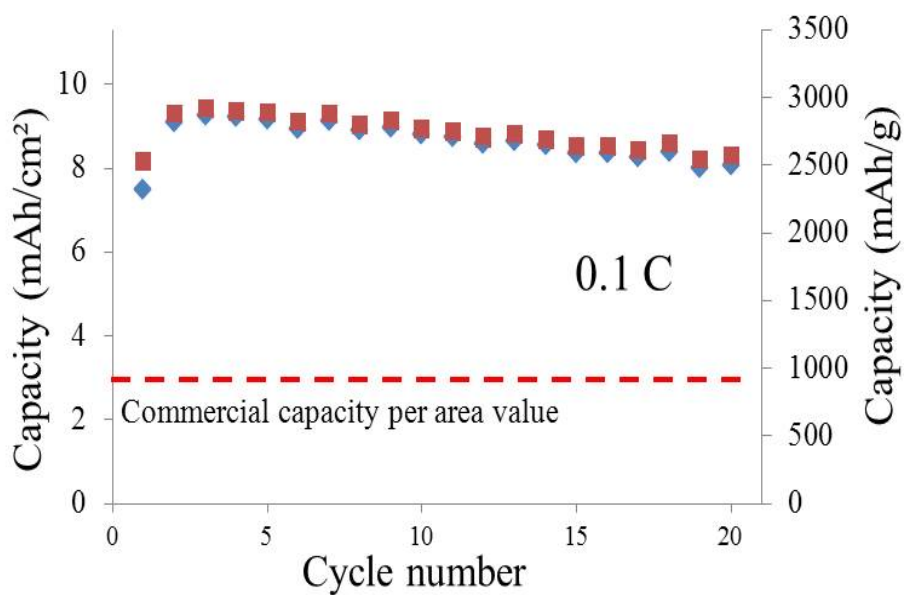
Figure 4.5 The capacity per area of a Si/CNT composite electrode with a thickness of 19.4 μm, a Si:CNT mass ratio of 51:1, and a volumetric silicon loading of 1.6 g/cm^3. Charge (square) and discharge (diamond) capacities at a rate of 0.1 C are shown versus cycle number

in the Fig. (4.6). However, a return to a lower C-rate resulted in a corresponding increase in the capacity back to the initial level.
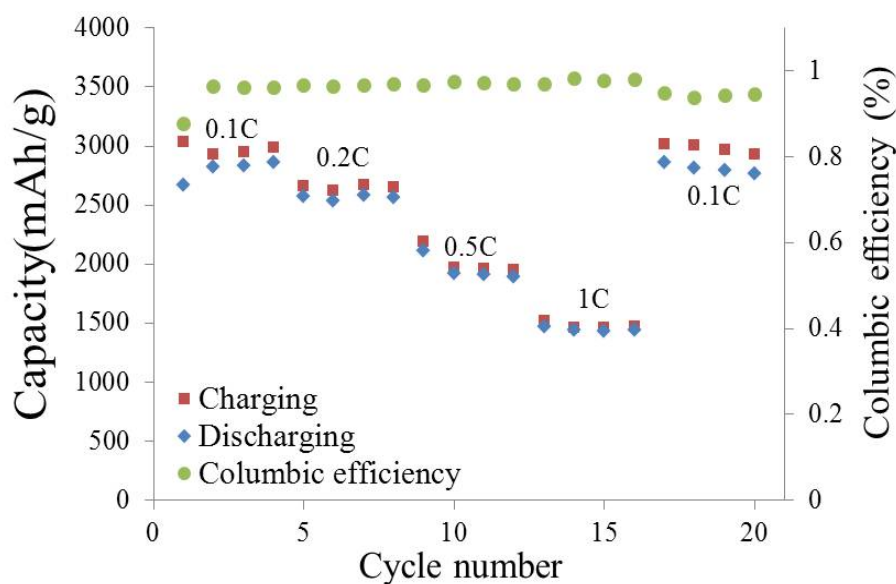
Figure 4.6 Specific capacity of a Si/CNT composite cycled at different C-rates. The composite has a thickness of 18.4 μm and a Si:CNT mass ratio of 35:1

Fig. (4.7) shows typical Nyquist plots of Si/CNT composites before and after cycling. The Nyquist plots are useful in identifying the kinetic contributions, for example, diffusion, convection, or migration. More details about Nyquist are shown in the discussion section and appendix. Before cycling, the ohmic resistance R is 13 Ω, the transfer resistance is around 1100 Ω, and the diffusion impedance angle is about 90° which is close to an ideal capacity. After a charging, R doesn't change and the transfer resistance did not change, but the diffusion impedance angle becomes 45°. However, the transfer resistance becomes small ~ 140 Ω.
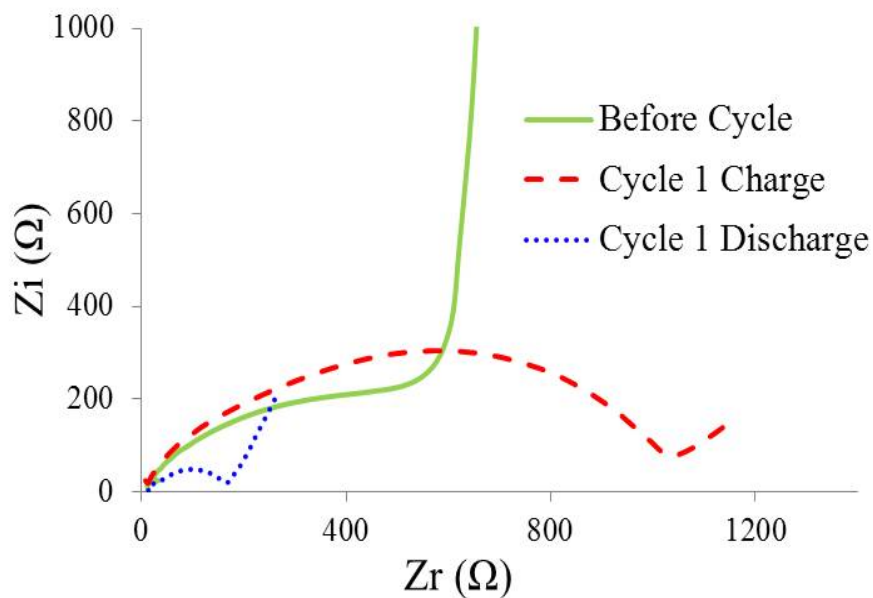
Figure 4.7 Nyquist plots for Si/CNT composites before and after cycling

4.4 Discussion and Conclusion

For high performance electrodes, capacity per area (and per volume) can be as important as capacity per mass. However, thicker electrodes often result in reduced specific and volumetric capacities due to the increasing electronic or ionic resistance. Our VACNT templated electrodes do not suffer from this trade-off over the range thicknesses considered.

It would be useful to know whether the high silicon per area loading and corresponding high areal capacities seen here can be even higher. The high areal loading comes from silicon's high volumetric capacity and the high silicon concentration in these electrodes. The high Si:CNT mass ratio (corresponding high volumetric capacity) is due to the small volume fraction (< 1 %) taken up by the CNTs and the high uniformity of the silicon infiltration.[93] Areal loading can be further increased by either increasing the thickness of nanocomposite electrodes or increasing the Si:CNT mass ratio. Fig. (4.3)a shows no significant decrease in specific capacity as the thickness is increased from 10 microns to 30 microns. This is

consistent with excellent silicon penetration during the infiltration of forests less than 50 microns tall, which results in uniform silicon shell thicknesses from top to bottom.[93] This also indicates that the capacities of these electrodes were limited by neither electron nor ion transport. This is likely due to the high electrical conductivity of the CNTs and the vertical nature of the resulting pores in the composite. We conclude that it should be possible to fabricate electrodes thicker than 30 microns to further increase areal capacity.

Our results showed no significant decrease in capacity (Cycle 4) as the Si:CNT mass ratio was increased from 9:1 to 84:1 (Fig. (4.3)b); however, silicon loadings higher than 60:1 showed severe fading problems (Fig. (4.4)c). A recent paper proposed a failure mechanism in nanostructured silicon anodes based on unstable SEI layers and continual SEI film growth that eventually blocks ion transport through porous anodes.[91] This explanation is consistent with our observations here; higher silicon loadings in our material will result in a shorter distance between silicon shells in the electrode yielding smaller pores for ion transport that are more readily blocked by SEI growth over time. The samples with thicker silicon shells likely have additional resistance associated with lithium ion diffusion in the solid, consistent with the rate data mentioned above; however, this is not expected to contribute to capacity fading during cycling.

For moderate loading, we see a large reversible capacity dependence on rate as shown in Fig. (4.6), indicating that irreversible SEI formation in the nanochannels is not the only significant rate limiting effect in this system. The columbic efficiencies observed in this study appear to be consistent with SEI growth on silicon.[90,97,98] Significant future work is required to fully understand and mitigate the rate limiting mechanisms and the role of SEI layers in these and other high surface area nanostructured electrode materials.

To evaluate the contribution of each component in electrochemical impedance spectroscopy (EIS) and to derive electrode characteristic parameters, we obtain Nyquist plots by

experiments as shown in Fig. (4.7). Now we compare an experimental plot to an equivalent circuit plot to explain the contribution of each component.

At high frequencies (above 10 kHz), the spectrum is dominated by the contribution of the connection resistance, including the electronic conduction between stainless steel and nanotubes, and the ionic conduction in electrolyte. According to our experimental results, no significant changes were observed in Re (from 10 to 20 Ω) throughout all the experiments for samples with various thicknesses and Si:CNT ratios.

As the frequency decreases (between 10 kHz and 10 Hz) each nanotube contributes to the surface resistance, which is due to electron transfer resistance (R_{ct}) on the electrode interface and the presence of a passivating SEI layer. This resistance is in parallel with a double layer capacitance (C_{dl}) and appears in the Nyquist plot as a depressed semicircle having a diameter equal to the value of the surface resistance. As discussed in Chapter 2, the silicon coating on individual CNTs is not uniform, resulting in various Si/CNT diameters. EIS performed in the work is not for individual Si/CNTs but for a Si/CNT forest, so the unmatched part as shown in Fig. (4.8) may be due to nonuniform Si/CNT diameters. The nonuniformity may result in a constant phase element in C_{dl}.[99]

At lower frequencies (below 10 Hz), the contribution from solid state diffusion is present, i.e., Li ions moving into the bulk of the Si/CNT composite. In this frequency region the diffusional impedance is large and a straight line of 45° slope is seen over the frequency range.

In conclusion, vertically aligned silicon-carbon nanotube composites fabricated directly on stainless steel substrates showed high specific, areal, and volumetric capacity. The composites consisted of multi-walled nanotubes covered with a uniform shell of amorphous silicon. The behavior of these nanocomposites as battery anodes was investigated for a wide range of silicon loadings; silicon to carbon mass ratio was varied from 9:1 to over 80:1. High, stable
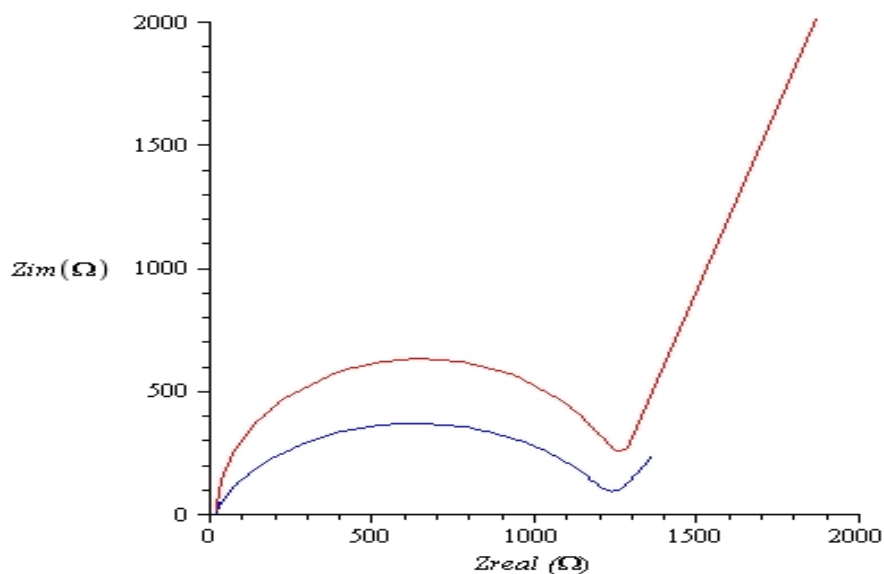
Figure 4.8 A typical experimental Nyquist plot for Si/CNTs
(blue) and a simulation plot from the equivalent circuit (red)

capacities up to 3000 mAh/g were seen in electrodes with Si:CNT mass ratios up to 50:1. Areal capacities greater than 9 mAh/cm^2 and volumetric capacities over 4600 mAh/cm^3 were achieved. This was done while maintaining a high specific capacity (2700 mAh/g). This combination of high gravimetric, volumetric, and areal capacity could make this an enabling materials system for high performance Li-ion batteries.

Chapter 5

Synthesis of Three Dimensional Patterned Silicon Carbide Nanowires

5.1   Introduction

Silicon carbide (SiC) has outstanding physical and mechanical properties including high thermal conductivity, high melting point, high mechanical strength, high electric breakdown field and excellent field emission properties.[100–102] Therefore, SiC is an ideal semiconductor material in extreme environments (i.e. high temperature, high power or high stress).[103,104] For potential applications in microelectronics and optoelectronics, one dimensional nanostructured silicon carbide nanowires (SiCNWs) have been synthesized by various methods such as: chemical vapor deposition (CVD),[105] laser ablation,[106] sol-gel,[107] vapor liquid solid,[108] and conversion of silicon coated carbon nanotubes.[109,110]

5.2 Fabrication of Three Dimensional Patterned Silicon Carbide Nanowires

We combine the conversion of silicon coated carbon nanotubes11 with a carbon nanotube templated microfabrication (CNT-M) process to demonstrate porous three dimensional microscale shapes consisting of silicon carbide nanowires (SiCNWs). The process is illustrated in Fig. (5.1). The CNT-M process uses partial material infiltration of patterned carbon nanotube frameworks to fabricate M-carbon nanocomposites with a wide variety of shapes and sizes.[65] Here "M" represents the material infiltrated into CNTs, for example, Si, C, Si_3N_4, metals etc. In this report, Si is infiltrated into the CNT pattern to form silicon-carbon core-shell nanotubes (Si/CNTs) and the Si/CNTs are then converted to SiCNWs by high temperature thermal annealing. The SiCNWs synthesized in controllable-length, large-quantity, and microscale shapes have potential applications in microelectronics and optoelectronics.

The fabrication process is illustrated in Fig. (5.1). The silicon wafer was patterned by photolithography and a lift-off procedure to produce a catalyst stack consisting of 30 nm of Al_2O_3 and 4 nm of Fe. Vertically-aligned CNT forests were grown from the patterned iron catalyst layer by thermal chemical vapor deposition (CVD). The vertical growth propagates the two dimensional patterning into a three dimensional structure. The feature sizes and shapes are determined by the lithography with features as small as a few microns to as large as several centimeters being achieved. Feature height is determined by the growth time. CNT growth was performed in a 1" tube furnace via the three step process as discussed in Chapter 2. Thin amorphous silicon was deposited onto the nanotubes by low pressure chemical vapor deposition (LPCVD) via the pyrolysis of silane in a 6" tube reactor. The silane flow rate was 20 sccm, the reactor temperature 530 °C, and the pressure 150 mTorr.

The Si/CNTs were then annealed at 1200 °C for 5 hours in argon.
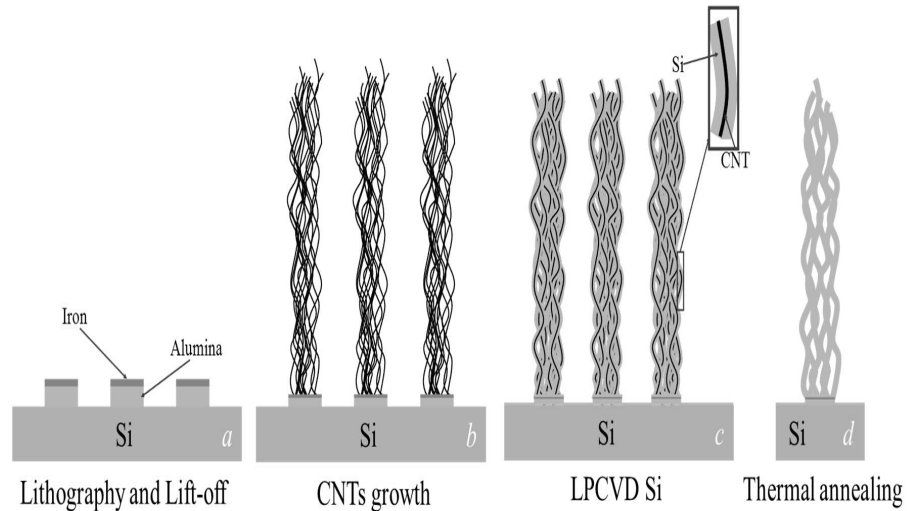
Figure 5.1 The fabrication diagram of three dimensional patterned SiCNWs. (a) The lithography (lift-off) is used to pattern the catalyst layer. The catalyst consists of iron and alumina. (b) CNTs grow only at the catalyst location. (c) Silicon is deposited on CNTs by the LPCVD process to form Si/CNTs. (d) Si/CNTs are converted to SiCNWs by thermal annealing

SEM images of a variety of patterned Si/CNTs are shown in Fig. (5.2). Depending on the lithography mask design, the pattern can consist of feature sizes from a few microns to centimeters as shown in Fig. (5.2)a. A variety of shaped Si/CNTs are shown in Fig. (5.2)b-d. The height of the synthesized Si/CNTs is controlled by controlling the run time for carbon nanotube growth: for example, a 2 min growth resulted in a $\sim$ 90 μm tall CNT forest (Fig. (5.2)c). After a silicon infiltration, the Si/CNT forest can retain the vertical orientation of the initial CNT forest even at a height 270 μm (fig Fig. (5.2)d).

SEM images of Si/CNTs before thermal annealing (Fig. (5.3)a and b) and after thermal annealing (Fig. (5.3)c and d) are shown in Fig. (5.3). The before and after images show the same microscale honeycomb patterns, however, the comparison of a rectangle bar structured Si/CNTs before annealing (Fig. (5.3)c) and after annealing (Fig. (5.3)d) shows a small
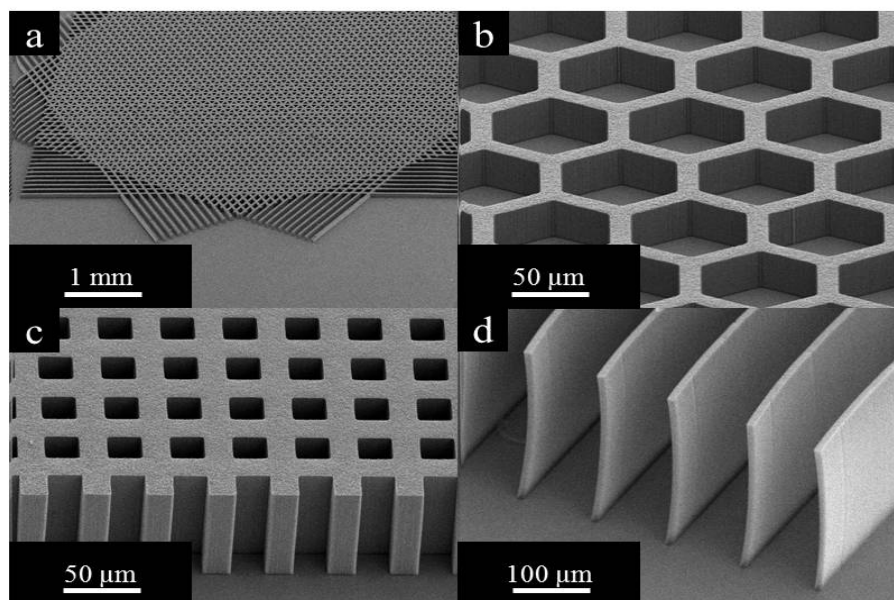
Figure 5.2 SEM images of Si/CNTs with various patterns and heights

expansion ($\sim$ 5 %) in the width.

The morphologies of individual CNTs, Si/CNTs, and SiCNWs are shown in Fig. (5.4). Fig. (5.4)a is an SEM image of as grown CNTs showing an average CNT diameter of $\sim$ 12 nm. Si/CNTs are shown in Fig. (5.4)b and d. The diameter of Si/CNTs can range from 12 nm to 120 nm dependent on the LPCVD deposition. A 40 minute Si deposition produced a $\sim$ 16 nm silicon shell on the individual CNT resulting in 44 nm diameter Si/CNTs (Fig. (5.4)b), while a 60 minute deposition resulted in a 72 nm diameter Si/CNTs (Fig. (5.4)d). Figure 4c and 4e show the annealed SiCNWs that correspond to the Fig. (5.4)b and Fig. (5.4)d starting point.
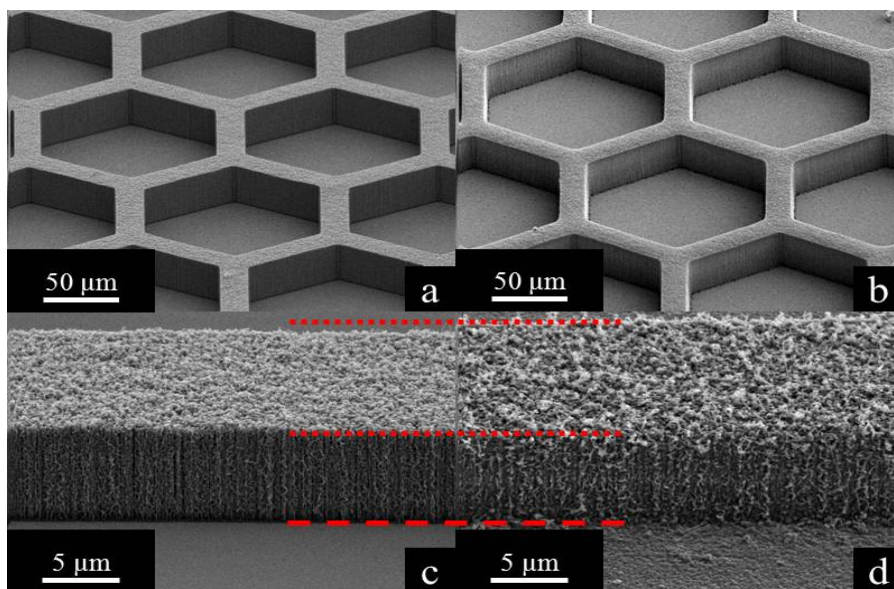
Figure 5.3 Patterned Si/CNTs (a,c) and patterned SiCNWs (b,d) are shown. (a) Honeycomb patterned Si/CNTs (b) Honeycomb patterned SiCNWs after the thermal annealing (c,d) A comparison of rectangle patterned Si/CNTs before annealing and after annealing. The dashed lines highlight the pattern variance
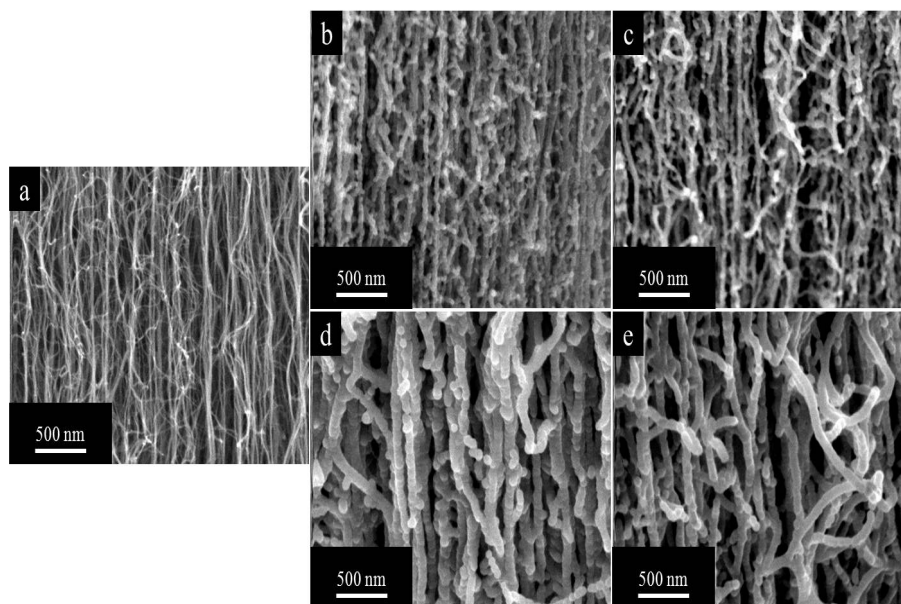
Figure 5.4 (a) A pristine CNT forest is shown. (b,c) A Si/CNT forest with 40 mins Si infiltration before annealing (b) and after annealing (c). (d,e) A Si/CNT forest with 60 mins Si infiltration before annealing (d) and after annealing (e)

5.3 Characterization of Silicon Carbide Nanowires

TEM and EELS analysis were used to investigate the nanoscale structure of the SiCNWs. A bright field/dark field pair of images is shown in Fig. (5.5). As seen in the SEM and TEM images, the overall "nanotube" type structure is retained. However, the CNTs were converted to the carbon component of SiC after the annealing process. The resulting structure seen in Fig. (5.5) consists of polycrystalline grains embedded in a matrix of amorphous material.

A STEM image with EELS analysis is shown in Fig. (5.6). The line in Fig. (5.6)a shows the region of an EELS line scan and the spectra (b,c) show typical examples of the silicon EELS spectra. Fig. (5.6)c shows the silicon spectra from the polycrystalline grain and Fig. (5.6)b is from the amorphous matrix. The EELS spectra from the amorphous edges of the wire show fine structure characteristic of silicon dioxide. In contrast, Fig. (5.6)c has
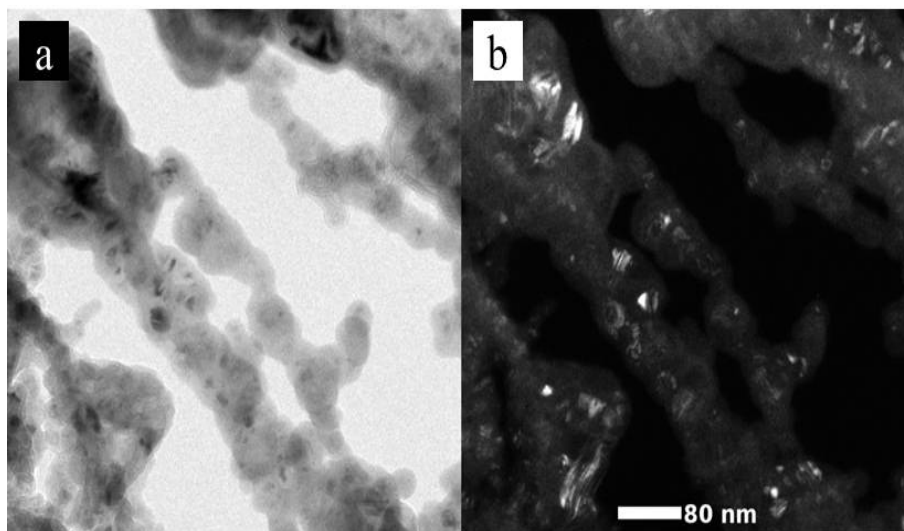
Figure 5.5 Bright and dark field TEM images showing several
wires with large grains. Twins are also clearly visible in many
grains, and the diffuse scattering in the dark field image is con-
sistent with an amorphous material

a different fine structure with the edge shifted approximately 4 eV lower than the silicon

dioxide. The fine structure and edge onset is consistent with SiC.[111] The silicon dioxide

matrix indicates oxygen contamination during the annealing. The contamination could have

arisen from a contamination of the argon gas or perhaps leakage due to the softening of the

quartz tube at 1200 °C.

The selected area electron diffraction (SAED) patterns from several nanowires is shown

in Fig. (5.7). A comparison of the measured d-spacings to reference values for β-SiC shows

a very good correspondence. The few percent deviation is within the expected error for this

TEM measurement.
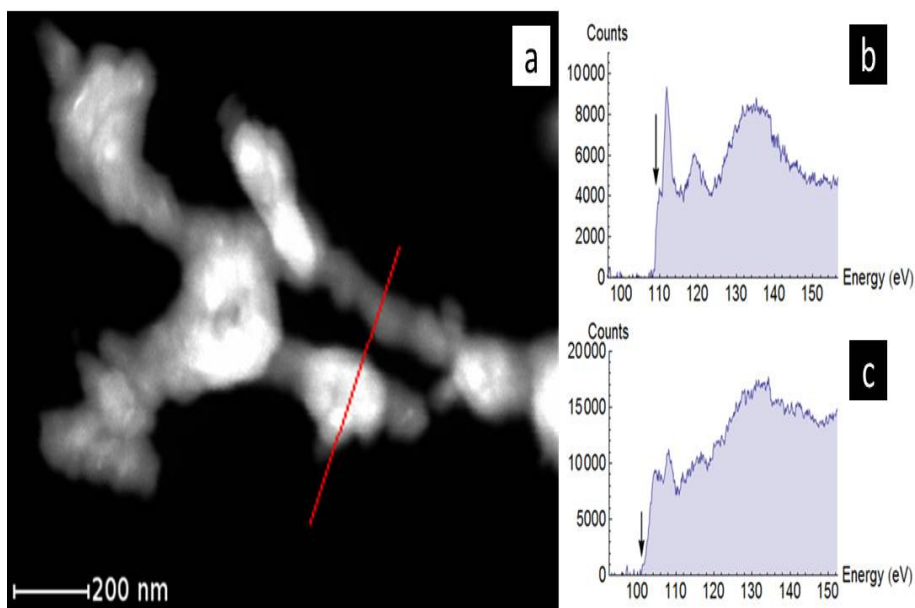
Figure 5.6 The red line in 6a indicates the scan path used to collect the Si EELS spectra. 6b and 6c show spectra taken at the edge (b) and center (c) of a wire
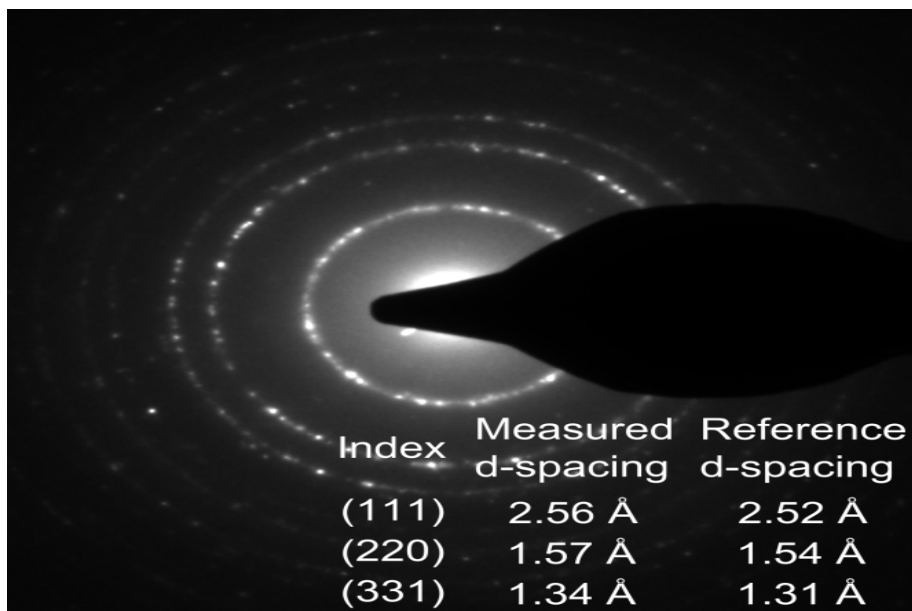
Figure 5.7 SAED Pattern with Comparison of measured d-spacings to β-SiC

5.4 Discussion and Conclusion

The experimental data shown for SEM, TEM, and EELS are consistent with the expected results of silicon carbide nanowires. The SiCNWs retain the original shape and orientation of the Si/CNT. The interior of the nanowires is marked by the presence of distinct polycrystalline grains covered by an amorphous SiO_2 coating. There are a large number of defects visible in the grains, and many of them exhibit twinning. No preferred orientation was observed among the grains. The silicon dioxide coating indicates an experimental oxygen contamination. One sample was subjected to a wet etch to remove the oxide layer and allow a more thorough analysis of the core. It was qualitatively found that the etching treatment decreased the strength of the nanowires based on how easy it was to break parts of the structure with tweezers. This would be expected based on the TEM images showing that the SiC grains were often poorly connected and thus cemented together with the silicon oxide matrix. The granular tubes that remained after etching did show clearer SiC EELS spectra and SAED patterns.

In conclusion, vertically aligned and patterned silicon carbide nanowires were fabricated by a CNT-M procedure consisting of a partial infiltration of silicon followed by a high temperature thermal annealing. The combination of CNT-M procedure and annealing resulted in three-dimensional patterned SiCNWs. The pattern was determined by the lithography and the diameter of SiCNWs was dependent on infiltration time and annealing time. The properties of SiCNWs were verified by SEM, TEM, and EELS.

Chapter 6

Conclusion and Future Work

6.1   Conclusion

I developed a carbon nanotube templated microfabrication (CNT-M) process to demonstrate porous three dimensional microscale shapes consisting of silicon-carbon core-shell nanotubes. The CNT-M process uses partial material infiltration of patterned carbon nanotube frameworks to fabricate M-carbon nanocomposites with a wide variety of shapes and sizes. Here "M" represents the material infiltrated into CNTs, for example, silicon, carbon, silicon nitride, metals, etc. In this work, I focused on nanocomposites resulting from silicon infiltration into VACNTs and their applications.

The heights of Si/CNTs are determined by the synthesis procedure of VACNTs, which can be from several microns to millimeters. The CNT-Si process resulted in an amorphous or crystalline silicon shell on the synthesized VACNTs. The uniformity of the shell is weakly dependent on depth of VACNTs, which are caused by a vapor concentration variance from top to bottom of VACNTs. Lower LPCVD temperatures and patterning gas access holes improve the gas transport and silicon infiltration uniformity. The Si/CNT diameters can be from 12 nm to 200 nm. In the former situation, there is little silicon coated on CNTs,

and the structure is mostly filled for a 200 nm diameter Si/CNT. Occasionally the silicon coating on CNTs forms separated beads along the CNTs. The bead formation may be due to insufficient coating, a smaller diameter of the underlying nanotube or a combination of two factors.

Silicon deposition temperatures ($>$ 500 °) can result in a sufficient mobility of silicon atoms to form beads of silicon on the multi-walled CNTs. Moreover, the higher temperatures ($>$ 560 °) produce a polysilicon structure and an amorphous silicon shell results from lower temperatures.

I view these 3-D porous structures as powerful testbeds for studying a variety of micro and nanostructured materials properties as well as chemical and physical processes on the micro and nanoscale. First, I applied the CNT-M process to fabricate silica nanowires for TLC that outperformed commercial HPTLC plates. The TLC plates provide chemical separations media with precise microscale channels for fluid flow control and nanoscale porosity for high analyte capacity.

Secondly, the CNT-M process was used to fabricate high capacity vertically aligned silicon-carbon nanotube composites directly on stainless steel substrates. The composites consisted of multi-walled nanotubes covered with a uniform coating of amorphous silicon. The behavior of these nanocomposites as battery anodes was investigated for a wide range of silicon loadings; silicon to carbon mass ratios were varied from 9:1 to over 80:1. High, stable capacities up to 3000 mAh/g were seen in electrodes with Si:CNT mass ratios up to 50:1. Areal capacities greater than 9 mAh/cm^2 were observed, which are high areal capacities with a good cycle stability. The volumetric capacity of the electrode was $\sim$ 4600 mAh/cm^3 which is about 20 times that of commercial lithium ion battery anodes ($\sim$ 230 mAh/cm^3). This combination of high gravimetric, volumetric, and areal capacity makes this an enabling materials system for high performance Li-ion batteries.

Last, the CNT-M procedure followed by a high temperature thermal annealing can fabricate three dimensional silicon carbide nanowires. The combination of CNT-M procedure and annealing resulted in three-dimensional patterned SiCNWs. The pattern was determinate by the lithography. The thermal annealing produced SiCNWs with a silicon oxide coating (due to oxygen contamination), and the diameter of SiCNWs was dependent on infiltration time and annealing time.

6.2 Future Work

In the application of thin layer chromatography, the precise microscale geometry with CNT-M provide an ideal test bed for future quantitative studies of the contribution of each term in van Deemter equation to efficiency.

In the application of lithium ion batteries, the cycle stability for higher silicon carbon nanotube mass ratios is still a problem. The possible reason is the formation and decomposition of SEI layers during charging and discharging. Significant future work is required to fully understand and mitigate the role of SEI layers in these and other high surface area nanostructured electrode materials.

There are broad areas that CNT-M procedure can be applied to such as catalysis, chemical separations, energy storage, energy conversion, biological and sensors. As a result, the metal infiltration into CNTs may be interesting, for example, in Microelectromechanical Systems (MEMS).

Bibliography

[1] G. Gao. Nanostructures and Nanomaterials - Synthesis, Properties and Applications, (World Scientific, 2004).

[2] P. Knauth and J. Schoonman. Nanostructured Materials: Selected Synthesis Methods, Properties and Applications. (Springer, 2002).

[3] A. Edelstein and R.C.Cammarata. 98 Nanomaterials: Synthesis, Properties and Applications. (Institute of Physics Publishing, 1998).

[4] G. C. David. Journal of Applied Physics. **93**, 793 (2003).

[5] X. Wang et al. Nano Letters. **9**, 3137 (2009).

[6] M. Monthioux and V.L.Kuznetsov. Carbon. **44**, 1621 (2006).

[7] B. Panymkeetal, et al. Russia Journal. **26**, 88 (1952).

[8] A. Oberlin and M. E., T. Koyama. Journal of Crystal Growth. **32**, 335 (1976).

[9] S. Iijima. Nature. **354**, 56 (1991).

[10] T. Durkop et al. Nano Letters. **4**, 35 (2004).

[11] J. Hone. Phonons and Thermal Properties. **80**, (2001).

[12] T. W. Ebbesen and P. M. Ajayan. Nature. **358**, 220 (1992).

[13] A. Thess et al. Science. **273**, 483 (1996).

[14] W.Z. Li et al. Science. **274**, 1701 (1996).

[15] T. Hiraoka et al. J. Am. Chem. Soc. **128**, 13338 (2006).

[16] M. Kumar and Y. Ando. Chem. Phys. Lett. **374**, 521 (2003).

[17] T. Yamada et al. Nature Nanotechnology. **1**, 131 (2006).

[18] H. Zhang et al. J.Phys.Chem.C. **112**, 12706 (2008).

[19] D. D. D. Ma et al. Science. **299**, 1874 (2003).

[20] J. D. Holmes et al. Science. **287**, 1471 (2000).

[21] C.K. Chan et al. Nature Nanotechnology. **3**, 31 (2007).

[22] A. M. Morales and C. M. L. Science. **279**, 208 (1998).

[23] M. D .Kelzenberg et al. Nano Letters. **8**, 710 (2008).

[24] E. C. Gamett, W. J. L, and P. D. Yang. Advanced Materials. **19**, 2946 (2007).

[25] D. P. Yu et al. Applied Physics Letters. **72**, 3458 (1998).

[26] X. Y. Zhang et al. Advanced Materials. **13**, 1238 (2001).

[27] Z. P. Huang, H. F., and J. Zhu. Advanced Materials. **19**, 744 (2007).

[28] G. Binnig, C. F. Q., and C. Gerber. Physical Review Letters. **56**, 930 (1986).

[29] D. Sarid. Scanning force microscopy with applications to electric, magnetic, and atomic forces. (New York, Oxford University, 1994).

[30] M. Knoll, Zeitschrift fr technische Physik. **16**, 467 (1935).

[31] O. C. Wells. Scanning Electron Microscopy. (New York, McGraw-Hill, 1974).

[32] M. Knoll and J. K. Subjective. Nature. **184**, 1823 (1959).

[33] M. Ohring. Materials Science of Thin Films. (Elsevier, 2002).

[34] R. J. Keyse. An introduction to scanning transmission electron microscopy. (Springer, 1998).

[35] J. I. Goldstein. Scanning Electron Microscopy and X-Ray Microanalysis. (Springer, 2003).

[36] J. Hillier and R. F. B. Journal of Applied Physics. **15**, 663 (1944).

[37] R. F. Egerton. Electron Energy-Loss Spectroscopy in the Electron Microscope. (Springer, 1996).

[38] G, Placzek. In: Hdb. der Radiologie. **2**, 209 (1934).

[39] D. J. Gardiner. Pratical Raman Spectroscopy. (Springer-Verlag, 1989).

[40] Thomas, Thackeray, and Whittingham. Science and Applications of Mixed Conductors for Lithium Batteries. (Materials Research Society, 2000).

[41] B. A. Boukamp, G. C. Lesh, and R. A. Huggins. Journal of The Electrochemical Society. **128**, 725 (1981).

[42] M. N. Obrovac et al. Journal of The Electrochemical Society. **154**, A849 (2007).

[43] S. Bourderau, T. Brousse, and D. M. J. Schleich. J. Power. Sources. **81**, 233 (1999).

[44] K. Yoshimura et al. J. Power. Sources. **146**, 445 (2005).

[45] H. Kim et al. Angewandte Chemie International Edition. **49**, 2146 (2010).

[46] D. Mazouzi et al. Solid State Lett. **12**, A215 (2009).

[47] M. Park et al. Nano Letters. **9**, 3844 (2009).

[48] L. Cui et al. Nano Letters. **9**, 491 (2009).

[49] T. Song et al. Nano Letters. **10**, 1710 (2010).

[50] K. Kang et al. Applied Physics Letters. **96**, 053110 (2010).

[51] L. F. Cui et al. Nano Letters. **9**, 3370 (2009).

[52] W. Wang and P. N. Kumta. Acs Nano. **4**, 2233 (2009).

[53] W. Wang, R. Epur, and P. N. Kumta. Electrochemistry Communications. **13**, 429 (2011).

[54] V. Meunier et al. Physical Review Letters. **88**, 075506 (2002).

[55] H. Bing, T. N., and R. Fred. Anal Chem. **70**, 3790 (1998).

[56] D. F. Perepichka and F. R. Small. **2**, 22 (2006).

[57] J. H. Lan et al. J Phys Chem C. **112**, 5598 (2008).

[58] S. Chakrabarti et al. J. Phys. Chem. C. **111**, 1929 (2007).

[59] C. Smit et al. Journal of Applied Physics. **94**, 3582 (2003).

[60] J. X. Liu et al. Physica E. **23**, 221 (2004).

[61] C. Lia et al. Physica E. **30**, 169 (2005).

[62] S. Nakashima, M. H., and K. Maeda. J Am Ceram. Soc. **86**, 823 (2003).

[63] J. Panitz and A. W. Applied Spectroscopy. **52**, 1252 (1998).

[64] P. M. Ajayan, S. I., and T. Ichihashi. Physics Review B. **47**, 6859 (1993).

[65] D. N. Hutchison et al. J Microelectromechanical Sys. **6**, 75 (2010).

[66] E. Dujardin et al. Science. **265**, 1850 (1994).

[67] B. Q. Wei et al. Nature. **416**, 495 (2002).

[68] S. R. Quake and A. S. Science. **290**, 1536 (2000).

[69] J. Erlebacher et al. Nature. **410**, 450 (2001).

[70] P. R. Bandaru, Journal of Materials Society. **42**, 1809 (2007).

[71] Z. G. Wu, J. B. N, and J. C. Grossman. Nano Letters. **9**, 2418 (2009).

[72] W. Wang and P. N. K. Acs Nano. **4**, 2233 (2010).

[73] J. W. Coburn and H. F. W. Ann Rev Marer Sci. **13**, 91 (1983).

[74] F. Marty et al. Microelectronics Journal, **36**, 673 (2005).

[75] S. Fan et al. Science. **283**, 512 (1999).

[76] K. Hata et al. Science. **306**, 1362 (2004).

[77] B. L. Wardle et al. Advanced Materials. **20**, 2707 (2008).

[78] Q. Ngo et al. Nano Letters. **4**, 2403 (2004).

[79] W. Q. Han et al. Science. **277**, 1287 (1997).

[80] B. C. Satishkumar et al. Journal of Materials Chemistry. **10**, 2115 (2000).

[81] W. Wang and P. N. K. Journal of Power Sources. **172**, 650 (2007).

[82] J. Y. Eom et al. Journal of Electrochemistry Society. **153**, A1678 (2006).

[83] M. Liu, G. H. L., and J. H. Chen. Nanotechnology. **19**, 265705 (2008).

[84] P. Gzil et al. Anal Chem. **75**, 6244 (2003).

[85] M. N. Obrovac and L. Christensen. Electrochem Solid St. **7**, A93 (2004).

[86] H. Chen et al. Journal of Solid State Electrochemistry. **14**, 1829 (2010).

[87] K. Kang et al. Applied Physics Letters. **96**, 053110 (2010).

[88] N. Choi et al. Journal of Power Sources. **161**, 1254 (2006).

[89] W. Xu and J. C. Flake. Journal of The Electrochemical Society. **157**, A41 (2010).

[90] Y. Guo, J. Hu, and L. Wan. Advanced Materials. **20**, 2878 (2008).

[91] Y. Oumellal et al. Journal of Materials Chemistry. **21**, 6201 (2011).

[92] R. Chandrasekaran et al. Journal of The Electrochemical Society. **157**, A1139 (2010).

[93] J. Song et al. Advanced Functional Materials. **21**, 1132 (2011).

[94] B. A. Johnson and R. E. White. Journal of Power Sources. **70**, 48 (1998).

[95] H. Guo et al. Materials Science and Engineering: B. **131**, 173 (2006).

[96] L. Hu et al. Advanced Energy Materials, **1**, 523, (2011).

[97] J. Graetz et al. Electrochemical and Solid-State Letters, **6**, A194 (2003).

[98] Q. Si et al. Journal of Power Sources. **189**, 761 (2009).

[99] R. Ruffo et al. J. Phys. Chem. C. **113**, 11390 (2009).

[100] T. Narushima et al. Mater. Trans. Jim. **38**, 821 (1997).

[101] S. Z. Wang et al. J. Inorg. Mater. **14**, 527 (1999).

[102] K. J. Watari. Ceram. Soc. Japan. **109**, S7 (2001).

[103] M. Mehregany et al. Int Mater Rev. **45**, 85 (2000).

[104] M. Willander et al. J. Mater.Sci. Mater.Electron. **17**, 1 (2006).

[105] Q. G. Fu et al. Mater. Chem. Phys. **100**, 108 (2006).

[106] W. S. Shi et al. J. Amer. Ceram. Soc. **83**, 3228 (2000).

[107] G. W. Meng et al. J. Mater. Res. **13**, 2533 (1998).

[108] S. Z. Deng et al. J. Chem. Phys. Lett. **356**, 511 (2002).

[109] C. C. Tang et al. Journal of Crystal Growth. **210**, 595-599 (2000).

[110] J. W. Liu et al. Chemical Physics Letters. **348**, 357-360 (2001).

[111] Gegner, J. Mat. - wiss. u. Werkstofftech (German). **34**, 203 (2003).

[112] F. J. Keil, R. Krishna, and M. O. Coppens. Rev. Chem. Eng. **16**, 71 (2000).

[113] M. Sahimi. Rev. Mod. Phys. **65**, 1393 (1993).

[114] M. Sahimi, G. R. Gavalas, and T. T. Tsotsis. Chem. Eng. Sci. **45**, 1443 (1990).

[115] G. F. Froment and K. B. Bischoff. Chemical Reactor Analysis and Design. (Wiley, New York, 1991).

[116] P. J. Gellings and H. J. M. Bouwmeester, The CRC Handbook of Solid State Electro-chemistry. (CRC Press, Boca Raton, Florida, 1997).

[117] F. J. Keil, Catal. Today.**53**, 245 (1999).

[118] L. F. Xu, M. Sahimi, and T. T. Tsotsis. Phys. Rev. E. **62**, 6942 (2000).

[119] S. K. Bhatia and J. S. Gupta. Rev. Chem. Eng. **8**, 177 (1992).

[120] J. D. Smet, et al. Journal of Chromatography A. **1073**, 43 (2005).

[121] P. Gzil, et al. Anal. Chem. **76**, 6707 (2004).

[122] S. Russ, et al. Physical Rev E. **72**, 030101(R) (2005).

[123] E. Barsoukov and J. R. Macdonald. Impedance Spectroscopy; Theory, Experiment, and Applications. (Wiley Interscience Publications, 2005).

[124] M. E. Orazem and B. Tribollet. Electrochemical Impedance Spectroscopy. (John Wiley and Sons, 2008).

[125] C. He, I. D. Raistrick and R. A. Huggins. J. Electrochem. Soc. **127**, 343 (1980).

Appendix A

Diffusion

In Chapter 2 or Chapter 3, we discussed solutes transferred from one place to another. For example, silane vapor diffuses from the top to the bottom of a CNT forest (Chapter 2), and analytes transport along a CNT-M TLC plate (Chapter 3). There are three transport mechanisms to transfer matter: migration, diffusion, and convection.[112] The three mechanisms are different from each other. Migration is a transport mechanism that applies only to ionic solutes exposed to an electromagnetic field. Diffusion of a solute results in different concentrations in adjoining regions, and diffusion is caused by the thermal motion and subsequent collisions of the molecules. Two types of diffusion can be distinguished: transport diffusion resulting from a concentration gradient, and self -diffusion which takes place in a system which is at equilibrium. Convection is the movement of molecules within solutes. There are two varieties of convection: neutral and forced. Neutral convection results from stray vibrations or from density gradients caused by temperature or a concentration differential. Forced convection arises from stirring the solution, bubbling gases, *etc*.

   Nanoporous materials were extensively used in technical applications, such as heterogeneous catalysis,[113–115] fuel cells,[116] adsorption,[117] and separations.[118] Many of these processes are diffusion controlled, so that a correct assessment of their efficiency depends on more ac-

curate determinations of the dependence of diffusion on the structure geometry. Effects of pore interconnections can be accounted for through methods such as percolation theory, the effective medium approximation, re-normalization group theory, and Monte Carlo simulations.[113, 114] Pore shape and surface morphology may also play a crucial role, which is typically ignored because of greater difficulties in modeling it realistically.[119]

The effective diffusivity of a solute within a porous medium is usually less than its value within bulk media. The phenomenon is known as "hindered" or "restricted" diffusion and it arises fundamentally from the fact that the characteristic dimension of the solute molecule is no longer small compared to that of the pore through which it passes. Several theoretical descriptions of solutes in porous structure have been developed.[84, 120, 121] The advantages of such physical models over phenomenological approaches, such as the based on non-equilibrium thermodynamics, is that they offer the possibility of predicting mass transfer rates from a limited number of independently measurable properties of the solute and porous barrier.

The diffusion of gas molecules through a porous medium depends on the collisions between the gas molecules as well as on the collisions of the gas with the pore walls.[122] In the transport pores, the so-called Knudsen diffusion dominates, where the interaction of the molecules with the pore walls play the crucial role and the intermolecular collisions can be neglected. In this case, the molecules perform a series of free flights and change the flight direction statistically after collisions with the pore walls.

In our discussion, we only consider diffusion in matter transport. A Fick's second law of diffusion gives:

$$\dot{c}/\dot{t} = D\ddot{\phi}/\ddot{x} \tag{A.1}$$

The time derivative of concentration is directly proportional to the second derivative of

concentration with respect to distance. The Fick's second law diffusion equation was used in Chapter 2. To explore the silicon infiltration, we model the infiltration process by using and revising the diffusion equation.

First we have:

$$0 = D\ddot{\phi}/\ddot{x} - \alpha\phi \tag{A.2}$$

Here ϕ is the concentration of the vapor. D is the diffusivity. Because the deposition time is long enough, the concentration profile should be time independent. Without the boundary conditions, the solution to the differential above is:

$$\phi = A\exp(\beta z) + B\exp(-\beta z) \tag{A.3}$$

(2-3) With the boundary conditions:

$$\phi_{z=0} = \phi_0 \tag{A.4}$$

$$\dot{\phi}_{z=h}/\dot{z} = 0 \tag{A.5}$$

we can get

$$A + B = \phi_0 \tag{A.6}$$

$$\beta(A\exp(\beta h) - B\exp(-\beta h)) = 0 \tag{A.7}$$

$$A = \phi_0/(1 + \exp(2\beta h)) \tag{A.8}$$

$$B = \phi_0 \exp(2\beta h)/(1 + \exp(2\beta h)) \tag{A.9}$$

Finally, the concentration is:

$$\phi = \phi_0(\exp(\beta z) + \exp(2\beta h - \beta z))/(1 + \exp(2\beta h)) \tag{A.10}$$

Appendix B

EIS Model

To elucidate the electrode process and to derive its characteristic parameters, we obtain Nyquist plots by using Electrochemical Impedance Spectroscopy (EIS).[123] EIS is a sensitive technique but it does not provide a direct physical explanation for the performance of an electrode. Electrochemical impedance is usually measured by applying an AC potential to an electrochemical cell and then measuring the current through the cell. We apply a sinusoidal potential excitation. The response to this potential is an AC current signal.[124]

The impedance is the ratio between the input potential and the output current signal. The impedance is represented as a complex number. If the real part is plotted on the X-axis and the imaginary part is plotted on the Y-axis of a chart, we get a "Nyquist Plot". Because the physical explanation can't be given directly by a EIS equipment, Nyquist plots are often used in the electrochemical literature because they allow for easy comparison with an equivalent circuit model.[123]

An equivalent circuit shown in Fig. (B.1) is used in analyzing the Nyquist plot.

Here R is the ohmic resistance including electronic resistance in the electrodes and ionic resistance in the electrolyte. R_{ct} is the charge transfer resistance between the electrolyte and the test electrode, formed by a kinetically controlled electrochemical reaction.
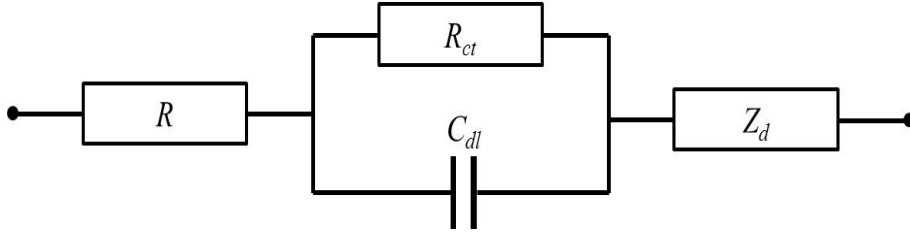
Figure B.1 An equivalent circuit of a Nyquist plot

C_{dl} is the double layer pseudocapacitance between electrolyte and test electrode. An electrical double layer exists on the interface between the test electrode and its surrounding electrolyte. This double layer is formed as ions from the solution enter the electrode surface. The charged electrode is separated from the charged ions.

Z_d represents the impedance element describing the diffusion process inside the electrolyte and test electrode. The diffusion is driven by a gradient in composition and not by an electric field, which creates an impedance called a Warburg impedance.[125] The impedance depends on the frequency of the potential perturbation. At high frequencies, the Warburg impedance is small since diffusing reactants don't have to move very far. At low frequencies, the reactants have to diffuse farther, increasing the Warburg-impedance.

So the total impendence Z_{tol},

$$Z_{tol} = R + (i\rho c + 1/R_{ct})^2 + (\sqrt[2]{i\rho}Y_0)^{-1}) = R + R_{ct}/((R_{ct}\omega c)^2 + 1) + \sqrt[2]{2}/(2Y_0\sqrt[2]{\omega}) - i((R_{ct})^2\omega c/((R_{ct}\omega c)^2 + 1) + \sqrt[2]{2}$$

(B.1)

To investigate the contribution of each part, we analyze each part of the total impedance. For example, if we only consider partial impedance Z_{part} which did not include diffusion impedance, we will get

$$Z_{part} = R + (i\rho c + 1/R_{ct})^2 = R + R_{ct}/((R_{ct}\omega c)^2 + 1) - i((R_{ct})^2\omega c/((R_{ct}\omega c)^2 + 1)) \quad \text{(B.2)}$$

Assume Z_r represents the impedance real part, Z_i represents the impedance imaginary part.

$$Z_r = R + R_{ct}/((R_{ct}\omega c)^2 + 1) \tag{B.3}$$

$$Z_i = (R_{ct})^2 \omega c/((R_{ct}\omega c)^2 + 1) \tag{B.4}$$

The relationship between impedance real part and imaginary part:

$$(I_m)^2 + (I_e - R - R_{ct}/2)^2 = (R_{ct})^2/4 \tag{B.5}$$
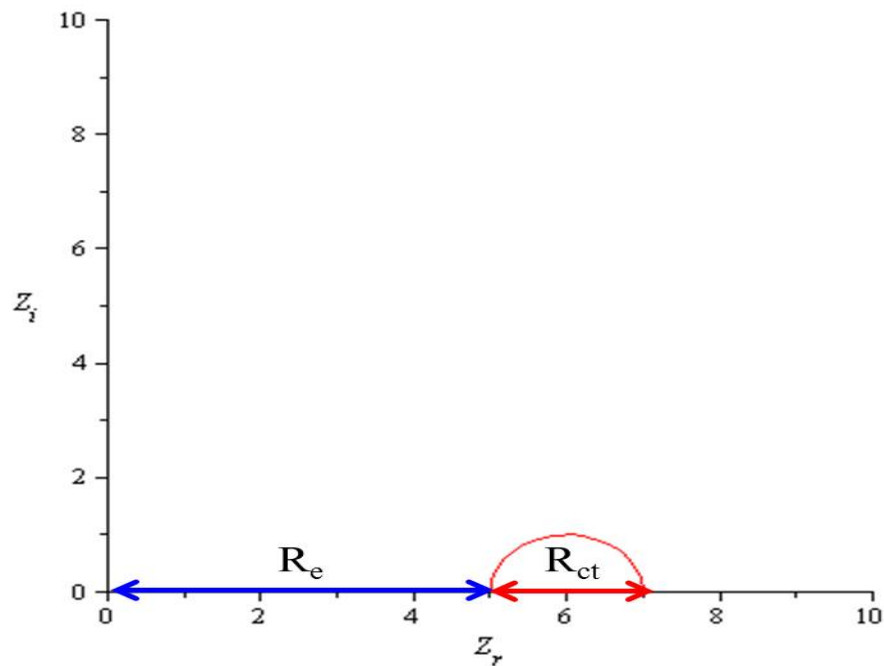

Figure B.2 A diagram shows the relationship between the impedance real part and imaginary part